Indication for clockwise rotation in the Siang window south of the eastern Himalayan syntaxis and new geochronological constraints for the area

URSINA LIEBKE[1]*, B. ANTOLIN[1], E. APPEL[1], N. BASAVAIAH[2], T. MIKES[3,4], I. DUNKL[3] & K. WEMMER[3]

[1]*Department of Geosciences, University of Tübingen, Sigwartstrasse 10, D-72076 Tübingen, Germany*

[2]*Indian Institute of Geomagnetism, Kalamboli Highway, New Panvel, Navi Mumbai 410218, India*

[3]*Geoscience Centre Göttingen, Goldschmidtstrasse 3, D-37077 Göttingen, Germany*

[4]*Present address: Institute of Geosciences, Goethe University Frankfurt, Altenhöferallee 1, D-60438 Frankfurt am Main, Germany*

**Corresponding author (e-mail: ursina.liebke@uni-tuebingen.de)*

Abstract: Palaeomagnetic, rock magnetic and geochronological investigations were carried out on the Abor volcanics of Arunachal Pradesh, NE India. A Late Palaeozoic formation age for part of the Abor volcanics cannot be excluded based on K–Ar whole rock dating. Low-temperature thermochronometers – zircon (U–Th)/He and fission track analyses – yield a maximum burial temperature of *c.* 150–170 °C during Late Miocene. ZFT thermochronology of the Yinkiong and Miri Fms. indicates a post-Paleocene and post-Jurassic deposition age, respectively. This infers that the volcanic rocks intercalating or intruding them are not part of the Late Palaeozoic sequence but represent one or more, latest Cretaceous to Tertiary event(s). Therefore the Abor volcanics are connected to at least two separate events of volcanism. From palaeomagnetic sites, two characteristic magnetic remanence components were separated: a low-coercivity-component demagnetized below 20 mT and a high-coercivity-component demagnetized between 15 and 100 mT. Fold tests support a secondary origin of both components. Thermochronological and rock magnetic analyses indicate a low-grade overprint event between India–Asia collision and Miocene, which probably represents the time of remanence acquisition. The high-coercivity-component shows a trend of clockwise declinations, which is likely related to vertical-axis rotations of the eastern Himalayas due to eastward extrusion of the Tibetan Plateau.

The Himalayan mountain range, created by collision of the Indian and Eurasian continents during Early Eocene, provides a unique opportunity for studying processes of continent–continent collision (Yin & Harrison 2000). The Himalaya extends between the Nanga Parbat Syntaxis at the western end and the Namche Barwa Syntaxis at the eastern end. The area around the Namche Barwa Syntaxis plays a key role in understanding geodynamic processes related to the eastward extrusion of the Tibetan Plateau. Ongoing indentation of India into Eurasia has led to considerable tectonic deformation of the Eurasian continent (Molnar & Tapponnier 1975). Clockwise tectonic rotations in the eastern part of the Himalayas are predicted by several numerical models and laboratory experiments in which the rigid Indian plate penetrates into the continuum of Asia (e.g. Houseman & England 1993; Beaumont *et al.* 2001; Cook & Royden 2008). Palaeomagnetic investigations on Cretaceous–Miocene rocks in the wider region north and west of the Namche Barwa Syntaxis supported these clockwise rotations (e.g. Otofuji *et al.* 1990, 1998; Funahara *et al.* 1992, 1993; Huang & Opdyke 1993; Sato *et al.* 1999, 2007; Yang *et al.* 2001). In addition, velocity vectors obtained from global positioning system (GPS) clearly display a clockwise rotational pattern around the Namche Barwa Syntaxis for the present aseismic surface movements (e.g. Chen *et al.* 2000; Mattauer 2002; Zhang *et al.* 2004; Shen *et al.* 2005; Sol *et al.* 2007). Most of the previous studies were performed north or east of the Namche Barwa Syntaxis. Due to political and infrastructural restrictions and very dense vegetation, the area south of the syntaxis is relatively unexplored. The present study provides new

From: Gloaguen, R. & Ratschbacher, L. (eds) *Growth and Collapse of the Tibetan Plateau.*
Geological Society, London, Special Publications, **353**, 71–97.
DOI: 10.1144/SP353.5 0305-8719/11/$15.00 © The Geological Society of London 2011.

palaeomagnetic and geochronological data on the Abor volcanic and adjacent sedimentary rocks of the Siang window in Arunachal Pradesh, NE India, located just south of the Namche Barwa Syntaxis. The age of the Abor volcanic rocks is highly controversial (e.g. Gansser 1964; Jain & Thakur 1978; Tripathi & Chowdhury 1983; Bhat 1984; Acharyya 1994, 2007; Kumar 1997). We present new geochronological and palaeomagnetic results that offer insight in the regional structure of the eastern Himalayan syntaxis area and the extrusion of the Tibetan Plateau.

Geological setting

The Arunachal Himalaya covers *c*. 350 km along strike of the eastern Himalayan fold-thrust Belt (Fig. 1) and extends from the eastern border of Bhutan to the Dibang and Lohit valleys at the eastern border of India. Many controversies exist about the classification, the distribution, and the age of rock units. Three of the main tectonostratigraphic units of the Himalayan orogen can be observed within the Arunachal Himalaya (Fig. 1b, c; Yin 2006). From north to south they are: the Greater Himalayan Crystalline Complex between the South Tibetan Detachment System (STDS) and the Main Central Thrust (MCT), the Lesser Himalayan sequence between the MCT and the Main Boundary Thrust (MBT), and the Siwaliks in the footwall of the MBT (Fig. 1; see Hodges *et al.* 2000; Yin 2006 for a review).

Figure 2a shows the main stratigraphic units of the eastern Arunachal Himalaya. In the eastern Himalaya, the MCT is broadly folded (e.g. Gansser 1983). Dating of monazite inclusions in garnet from the MCT zone in western Arunachal indicates

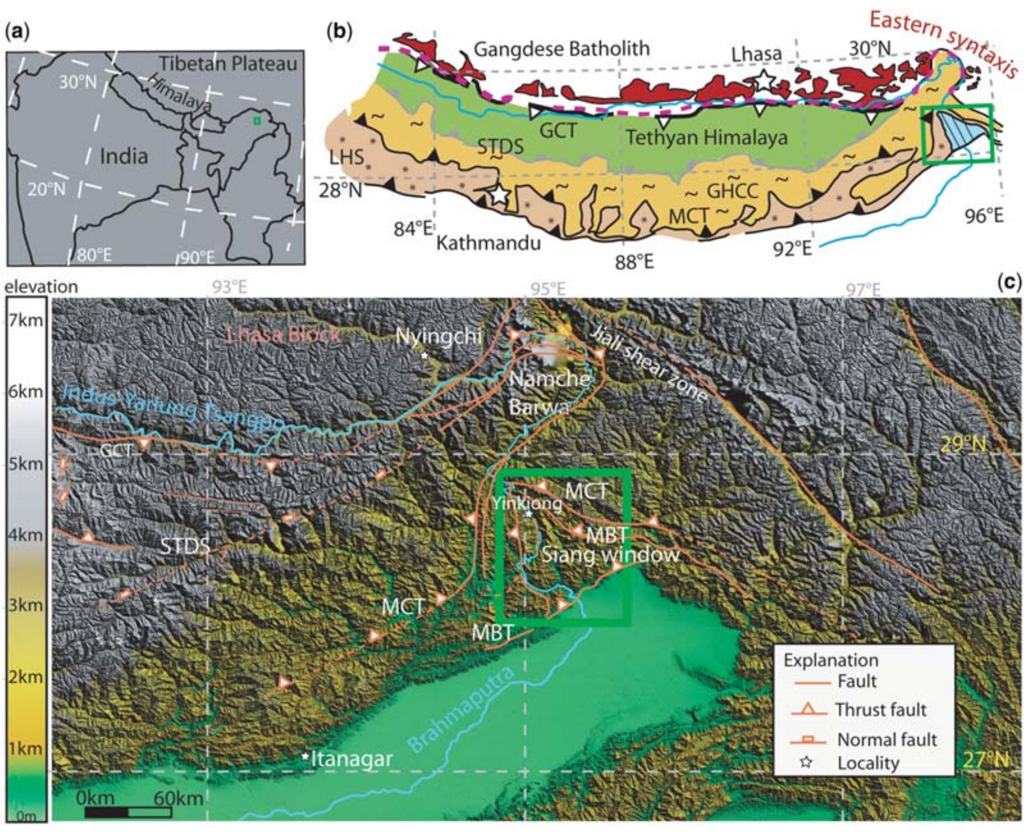

Fig. 1. The study area (green box) at three different scales: (**a**) Sketch of India and surrounding regions; (**b**) Simplified geological map of the Himalaya (modified after Ding *et al.* 2001; Pan *et al.* 2004; Yin *et al.* 2006). (**c**) Relief map (http://srtm.csi.cgiar.org/) around the Siang window with approximate trace of the main structural elements from Ding *et al.* (2001) and Acharyya (2007). MBT, Main Boundary Thrust; MCT, Main Central Thrust; STDS, South Tibetan Detachment System; GCT, Great Counter Thrust; LHS, Lesser Himalayan Sequence; GHCC, Greater Himalayan Crystalline complex; rectangle shows study area.

that the MCT was active *c*. 10 Ma ago (Yin *et al.* 2006). The Se La Group between the STDS and the MCT consists of high grade gneisses and schists of the Greater Himalayan Crystalline Complex. The STDS is well recognized further east in the Siang river section (Acharyya & Saha 2008). The Lesser Himalaya is composed of the Late Proterozoic Bomdila Group and the Late Palaeozoic Lower Gondwana Group. In the eastern part of Arunachal Pradesh the Lesser Himalaya is made up of mostly Phanerozoic rocks (Kumar 1997). The Neogene–Early Quaternary molasse-type sediments in the footwall of the Main Boundary Thrust (MBT) belong to the Siwaliks (Kumar 1997).

The Siang window: tectonostratigraphy

The present study focuses on the Abor volcanic rocks which crop out at the core of the Siang window. The Siang window encompasses *c*. 8000 km^2 of the eastern part of the Arunachal Himalaya (Figs 1a, c & 2a). According to several authors (e.g. Sengupta *et al.* 1996; Gururajan & Chowdhury 2003; Acharyya 2007), the Siang window comprises antiformally folded and up-arched thrust sheets, which are made of Lesser Himalayan rocks (Fig. 2b). It has been proposed that the window was evolved during the process of southward exhumation of the Greater Himalayan Crystalline Complex and south-vergent thrusting over the Tertiary Himalayan foreland basin (Acharyya 1998; Acharyya & Sengupta 1998). The antiformal duplex structure, which breached the MBT and passively folded overlying Himalayan nappes, was possibly formed by compressive tectonics at the Eastern Syntaxis (Acharyya 2005). Two sedimentary units are exposed at the core of the Siang window: the upper Yinkiong Fm and a lower unit (Miri Fm) composed of mainly white quartzites with occasionally coarser bands containing jasper. The Yinkiong Fm is composed of an alternating sequence of dark grey sandstone to siltstone and green and red shale with rare orthoquartzites and volcanic rocks (Jain & Tandon 1974). Its foraminiferal assemblage indicates an Early to Mid Eocene age (Acharyya 1994). The quartzites of the lower unit were lithostratigraphically correlated with the Middle Palaeozoic to Lower Permian Miri Quartzite exposed in adjacent areas (Jain & Thakur 1978; Bhat 1984). Acharyya (1994) reported a foraminiferal assemblage from limestone bands in the upper part of the quartzites and proposed a Palaeogene age for at least this upper part of the Miri Fm. The Abor volcanic rocks are exposed as lava flows, sills, dykes, volcanic breccias, and metatuffs (Jain & Thakur 1978) and comprise hard, massive, or amygdaloidal basaltic to andesitic rocks. Thin section petrography of our samples reveals rather fresh feldspar and clinopyroxene phenocrysts. Formation of chlorite and epidote locally in the glassy matrix indicates a weak post-emplacement hydrothermal and/or diagenetic transformation of the volcanic rocks (Fig. 3).

Locally, the rock units within the window are dissected by several subsidiary normal faults oblique to both, the MBT and the North Pasighat Thrust (NPT) (Kumar 1997; Acharyya 2007). They are bound by the Bomdila Group to the north, east and west. To the south, the rocks units of the Siang window are truncated against Neogene Siwaliks sediments across the NPT (Fig. 2; Kumar 1997; Acharyya 2007).

Previous age constraints of the Abor volcanic rocks

Age and evolution of the Abor volcanic rocks have been a matter of great controversy. Based on lithological and geochemical similarities, many authors correlated them to the Permo-Triassic Panjal Trap volcanism (e.g. Gansser 1964; Bhat 1984; Bhat & Ahmad 1990; Kumar 1997), associated with the break-up of Gondwana. Jain & Thakur (1978); however, assumed a Precambrian to Middle Palaeozoic age for the volcanic rocks. Their arguments were based on: (a) the NNW–SSE structural trend of the lithological units within the Siang district, which is thought to be connected to the Mid Palaeozoic orogeny in this part of the Himalayas; (b) the presence of quartzite, slate, basalt, and other rock fragments in diamictites of the Gondwana belt, interpreted to have been derived from the Miri-Siang Group and the Abor volcanic rocks; and (c) agglomeratic volcanic rocks and tuffs intercalating pebbly mudstones assigned to the Gondwana belt in the NE Himalaya. These arguments have been challenged early on by Chowdhury (1979) on basis of biostratigraphical and structural data. Gansser (1974) and Le Fort (1975) have also cast doubt on a Mid Palaeozoic orogeny in this area.

Tripathi *et al.* (1979, 1981*b*) were the first to report Early Eocene foraminifera and plant imprints closely associated with the Abor volcanic rocks and from the Yinkiong Fm. This was supported by the discovery of Upper Paleocene to Lower Eocene nummulitic limestones in the Yinkiong Fm (Tripathi *et al.* 1981*a*). In other sections, marine molluscs and sporomorph assemblages of Gondwana affinity document a Permian age for the sedimentary rocks associated with the volcanic formations (e.g. Singh 1981; Tripathi & Chowdhury 1983; Sinha *et al.* 1986; Prasad *et al.* 1989). It has therefore been assumed that two different sets of volcano-sedimentary sequences occur in the Siang window, an Early Tertiary and a Permian one (e.g. Singh 1984; Singh & De 1984; Singh & Malhotra

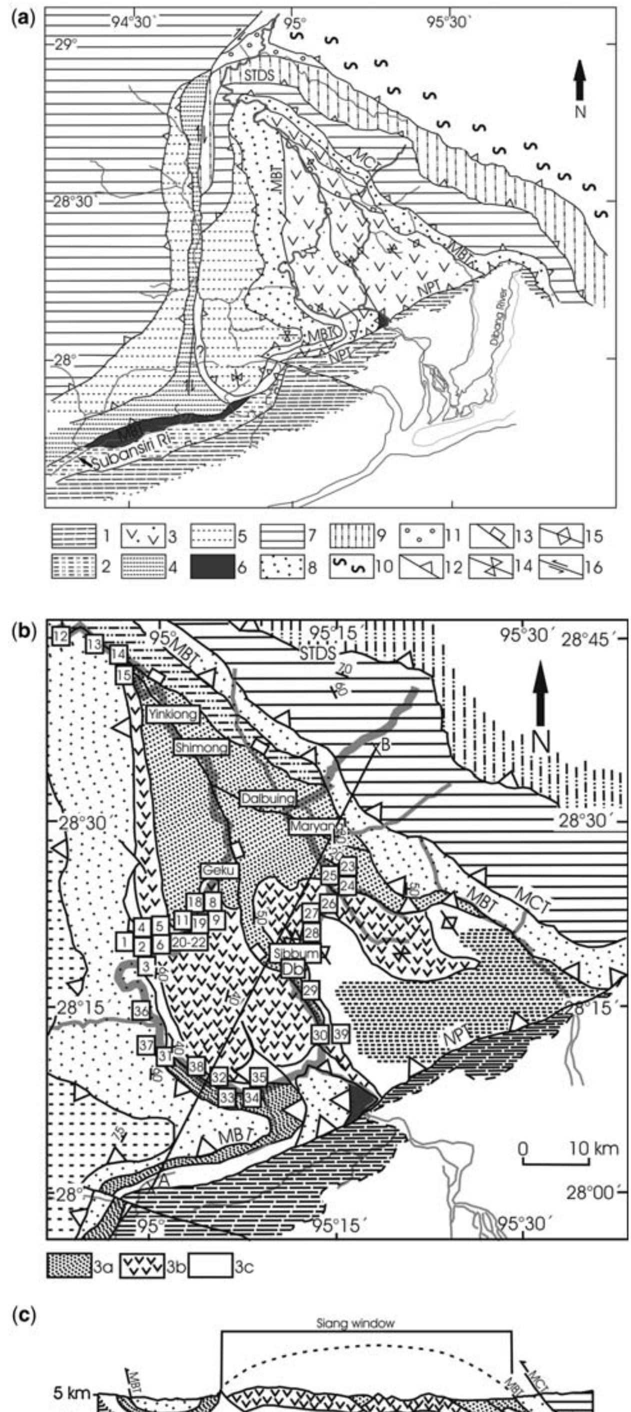
(a)
94°30´
95°
95°30´
29°
28°30´
28°
STDS
MCT
MBT
NPT
N
Subansiri R.
Dibang River
1
2
3
4
5
6
7
8
9
10
11
12
13
14
15
16
(b)
95°
95°15´
95°30´
28°45´
28°30´
28°15´
28°00´
28°
STDS
MBT
MCT
NPT
N
Yinkiong
Shimong
Dalbuing
Maryang
Geku
Sibbum
Db
A
B
0 10 km
3a
3b
3c
(c)
Siang window
5 km
0 km
-5 km
-10 km
MBT
MCT
main detachment fault

Fig. 2.

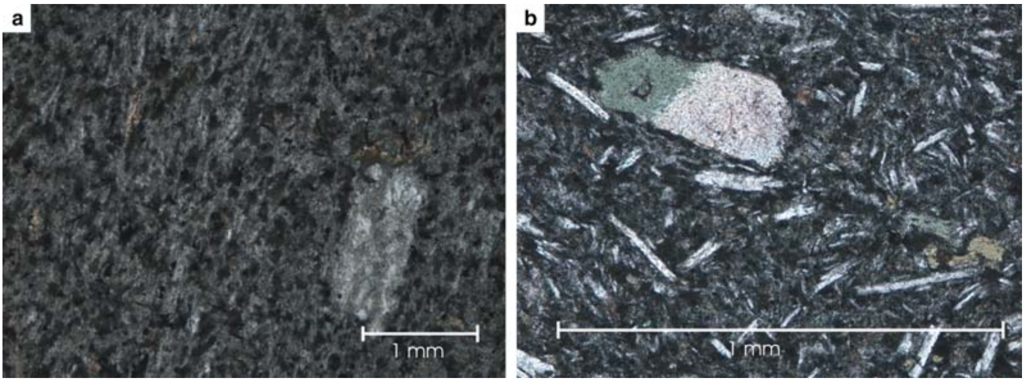

Fig. 3. Photomicrographs of thin sections. (**a**) glassy groundmass of sample AbV-24; (**b**) chloritization of a clinopyroxene in sample AbV-1.

1987). Tripathi *et al.* (1988) also postulated two different units of the Abor volcanic rocks: an older Permian unit exposed around Rotung and a younger Eocene unit exposed around Geku. However, mapping revealed that these units join together (Singh 1993). A slate boulder with Permian marine bivalves was reported close to the Dalbuing area, whereas Lower–Mid Eocene foraminifera were recorded from the Yinkiong Fm (Sinha *et al.* 1986; Singh 1993). According to Acharyya (1994, 2007) the deformed slate with Permian fossils possibly occurs as a thrust sliver close to the MBT and NE of Dalbuing.

Acharyya (1994) dated calcareous quartzites and limestone bands directly underlying the Abor volcanic rocks to be Late Paleocene–Early Eocene in age by larger foraminifera. According to him, the Abor volcanic rocks were erupted in-between the deposition of the Late Paleocene–Early Eocene quartzites and the Yinkiong Fm and therefore range in age from Upper Paleocene–Early Eocene. If this scenario is valid, volcanism would be fairly contemporaneous with the collision of the Indian and Asian plates during Early Eocene probably triggered by either adiabatic decompression following crustal thickening (Sengupta *et al.* 1996) or the thermal anomaly related to slab break-off following the collision (Acharyya 2007).

Sample treatment and analytical procedures

Core samples from 35 sites were drilled with a portable rockdrill. Orientation was generally recorded by a magnetic compass; no sun compass was required because of the relatively low remanence intensity. The core samples were cut into standard specimens of 2.5 cm diameter and 2.2–2.3 cm length. Palaeo- and rock magnetic measurements were carried out at Tübingen University; geo- and thermochronological analyses were performed at Göttingen University.

The natural remanent magnetization (NRM) of two pilot samples (twin samples) was demagnetized by alternating field and thermal treatment. Remanence directions were measured using a 2 G Enterprises SQUID magnetometer 755R. Alternating

Fig. 2. (**a**) Simplified map of the Siang window (modified after Acharyya & Saha 2008). 1, Upper and Middle Siwaliks; 2, Lower Siwaliks; 3, Rocks exposed at the core of the Siang window (undifferentiated); 4, Miri Quarzite; 5, Low-medium grade meta-argillite (Proterozoic); 6, Late Palaeozoic metasediments of the Lower Gondwana Group; 7, High grade rocks and gneisses of the Greater Himalayan Crystalline Complex (Se La Group); 8, Bombdila Group (low-grade quartzite-dolomite metasediments of the Buxa Fm); 9, Yang Sang Chu Fm (Proterozoic); 10, Trans-Himalayan granitoids and gneisses; 11, Mafic and ultramafic rocks (ophiolites). Structural features: 12, Major thrust; 13, Fault; 14, Axial trace of synclinal fold; 15, Axial trace of anticlinal fold; 16, Strike–slip fault. Abbreviations: MCT, Main Central Thrust; MBT, Main Boundary Thrust; NPT, North Pasighat Thrust; STDS, South Tibetan Detachment System. The Dibang and Lohit Valleys are located off the map further east. (**b**) Geological map of the core of the Siang window showing palaeomagnetic site locations of this study and position of geochronology studied site Db (‘drift boulder’). The map was modified after Acharyya & Saha (2008); structural data are taken from Singh (1993). The legend is the same as in Figure 2a; rocks exposed at the core of the Siang window are differentiated to: 3a, Yinkiong Fm; 3b, Abor volcanic rocks; 3c, Quartzites. Note that all palaeomagnetic sites were sampled from the Abor volcanic rocks; the location of some sites within different stratigraphic units is either due to imprecise drawing of the map or imprecise GPS data. (**c**) Structural cross section along AB (modified after Acharyya 2007).

field demagnetization (AfD) was performed using an automatic 3-axes degaussing system integrated in the SQUID magnetometer; 15 steps with a maximum applied field of 100 mT were applied. For thermal demagnetization (ThD) 13 steps with 25–100 °C temperature increments and a maximum temperature of 700 °C were performed. Heating was done in an ASC scientific furnace (model TD-485 C). In order to detect possible changes in the magnetic mineralogy, the bulk magnetic susceptibility was measured after each step of heating using a Kappabridge KLY-2 (Agico). The demagnetization results indicate that both AfD and ThD are suitable to separate remanence components. As AfD is more convenient, the natural remanent magnetization (NRM) of eight to nine specimens per site was progressively demagnetized by alternating field cleaning. In addition, ThD of NRM was applied to eight specimens of five sites in order to relate magnetic components to specific ferro(i)magnetic minerals.

To determine the magnetic mineralogy one specimen of 19 representative sites was applied to stepwise acquisition of isothermal remanent magnetization (IRM) using a pulse magnetizer MMPM9 (Magnetic Measurements Ltd) with a maximum field of 2.5 T. The intensity of IRM was measured with a Minispin spinner magnetometer (Molspin Ltd). Subsequently, the IRM of three orthogonal components (Lowrie 1990) was thermally demagnetized. Susceptibility v. temperature curves from room temperature to maximum 700 °C were measured for 20 specimens using a CS-3 heating device coupled with a Kappabridge KLY-3 (Agico). Anisotropy of magnetic susceptibility (AMS) was measured for three sites using Kappabridge KLY-2. The saturation IRM (SIRM) of eight specimens per site was determined (using the Minispin) after applying a magnetic field of 2.5 T.

For zircon thermochronology the samples were crushed, sieved and treated by the common heavy liquid and magnetic separation processes. The zircon crystals were embedded in PFA Teflon and polished in five steps by diamond suspensions and etched by the eutectic melt of NaOH–KOH at a temperature of 220 °C. Neutron irradiations were performed in the research reactor of the Technical University of Munich (Garching). The external detector method was used (Gleadow 1981). After irradiation the induced fission tracks in the mica detectors were revealed by etching in 40% HF for 40 min at 21 °C. Track counting was made with a Zeiss-Axioskop microscope-computer-controlled stage system (Dumitru 1993), with 1000× magnification. The FT ages were determined by the zeta method (Hurford & Green 1983) using age standards listed in Hurford (1998). The error was calculated by using the classical procedure, that is, by double Poisson dispersion (Green 1981). Calculations and plots were made with the TRACKKEY program (Dunkl 2002).

For zircon (U–Th)/He chronology single crystal aliquots were dated; only intact, euhedral crystals with minor inclusions were selected. The shape parameters were measured and archived by multiple microphotographs; the alpha ejection factors (Ft, see in Farley *et al.* 1996) were determined by the constants of Hourigan *et al.* (2005). The crystals were wrapped in *c.* 1 × 1 mm-sized platinum capsules and degassed in high vacuum by the heating of an infra-red diode laser (Reiners 2005). The extracted gas was purified using a SAES Ti–Zr getter at 450 °C. The chemically inert noble gases and a minor amount of other rest gases were then expanded into a Hiden triple-filter quadrupol mass spectrometer equipped with a positive ion counting detector. Beyond the detection of helium the partial pressures of some rest gases were continuously monitored (H_2, CH_4, H_2O, Ar, CO_2). He blanks (*c.* 0.0003 and 0.0008 ncc ^{4}He) were estimated using the same procedure on empty Pt tubes (cold and hot blanks, respectively). Crystals were checked for degassing of He by sequential reheating and He measurement. Following degassing, samples were retrieved from the gas extraction line, spiked with calibrated ^{230}Th and ^{233}U solutions, and dissolved in pressurized Teflon bombs using distilled 48% HF + 65% HNO_3 in five days at 220 °C (applying a slightly modified procedure of Evans *et al.* 2005). Spiked solutions were analysed by isotope dilution method using a Perkin Elmer Elan DRC II ICP-MS equipped with an APEX micro-flow nebulizer. Sm, Pt and Zr concentrations were determined by external calibration. The oxide formation rate and the PtAr–U interference were always monitored, but their effects were negligible on the concentration of actinides.

For K–Ar dating the samples were carefully cleaned and selected in order to avoid altered parts or veins. The selected pieces were crushed and gently pulverized in a ball mill to reach an appropriate grain size of approx. 100 μm to prevent the loss of Ar during preparation. In case of the shale sample, the <2 μm and <0.2 μm size fractions were separated from suspension by gravity settling (Stokes' Law) and ultra-centrifugation. The samples investigated suffer from a trapped, atmospheric contamination (up to 70% of the ^{40}Ar) which can not be avoided in most volcanic rocks (s. discussion in McDougall & Harrison 1999). Therefore, errors amount up to 4.6% (2σ). The argon isotopic composition was measured in a Pyrex glass extraction and purification line coupled to a VG 1200 C noble gas mass spectrometer operating in static mode. The amount of radiogenic ^{40}Ar was determined by isotope dilution method using a highly enriched ^{38}Ar spike from Schumacher, Bern (Schumacher 1975). The spike is calibrated against the biotite standard HD-B1 (Fuhrmann *et al.* 1987). The age calculations are based on the constants recommended by the IUGS quoted in Steiger & Jäger (1977). Potassium was determined in duplicate by flame photometry using an Eppendorf Elex 63/61. The samples were dissolved in a mixture of HF and HNO_3 according to the technique of Heinrichs & Herrmann (1990). CsCl and LiCl were added as an ionization buffer and internal standard, respectively. The analytical error for the K–Ar age calculations is given on a 95% confidence level (2σ). Details of argon and potassium analyses for the laboratory in Göttingen are given in Wemmer (1991).

Results

Rock magnetic results

Magnetic mineralogy could be deduced from IRM acquisition curves, thermal demagnetization of three-component IRM, and the thermo-magnetic behaviour of susceptibility. Results from representative samples prove magnetite, Ti-rich titanomagnetite, and hematite as the dominant ferro(i)magnetic minerals. High temperature thermomagnetic runs were done for powdered samples and crushed samples. Powdered samples were ground to a fine rock powder, whereas crushed samples consisted of rock particles with diameters of about 2–5 mm. Heating curves of powdered samples reveal magnetite by a decrease in magnetic susceptibility just below its Curie temperature (Fig. 4a). Cooling curves are partly irreversible indicating oxidation of magnetite to hematite during heating; deviating Curie temperature during heating and cooling can be related to temperature hysteresis due to different heat capacities of the sample and the thermoelement. Heating curves of crushed samples show an additionally decrease below 400 °C (Fig. 4b), probably caused by Ti-rich titanomagnetite. Because Ti-rich titanomagnetite is only meta-stable at room temperature and collapses on application of mechanical stress or heating (O'Reilly 1984), it has been likely destroyed during grinding of the powdered samples.

For analysis of IRM acquisition curves, the irmunmix2_2_1 and IRM_CLG1 software (Kruiver *et al.* 2001) were utilized, which are based on cumulative log-Gaussian analysis (CLG). By means of

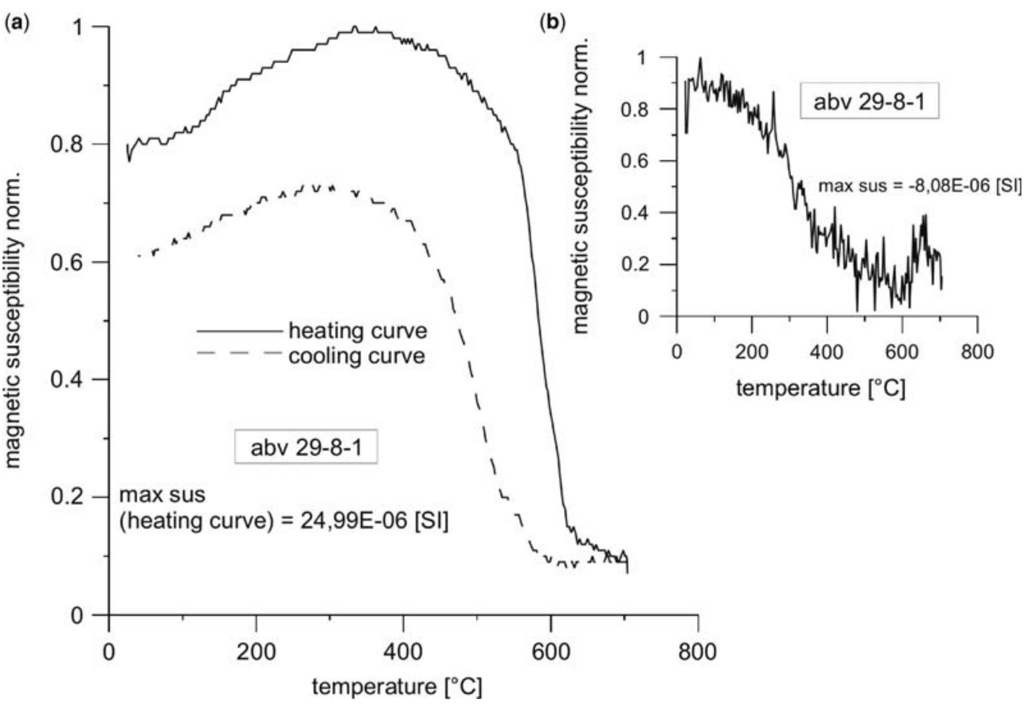

Fig. 4. Susceptibility v. temperature curves of abv 29–8–1; (**a**) heating and cooling curve of a powdered sample; (**b**) heating curve of a crushed sample; the noisy character of the heating curve is probably due to relatively high volume differences in the rock particles. Max sus, maximum susceptibility.

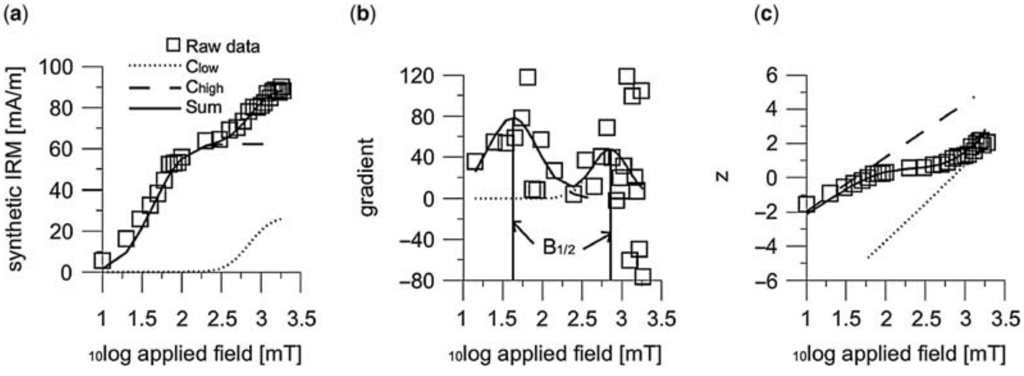

Fig. 5. Results of Cumulative log-Gaussian analysis of abv 19–9–1; (**a**) linear IRM acquisition plot; (**b**) gradient acquisition plot; (**c**) standardized acquisition plot.

these programs coercivity parameters of different components are approximated by the applied magnetic field which causes half of the SIRM to be acquired ($B_{1/2}$). IRM acquisition curves and ThD of three-component IRM show variable results for different samples reflecting the complex rock and palaeomagnetic behaviour. Three different components were distinguished based on their coercivity spectra (Fig. 5, Table 1) and blocking temperatures. A low coercivity component (C_{low}) was defined by $B_{1/2}$ values below 70 mT. $B_{1/2}$ values between *c*. 70 and 100 mT were allocated to an intermediate coercivity component (C_{int}) and $B_{1/2}$ values above 380 mT to a high coercivity component (C_{high}). IRM acquisition curves and thermal demagnetization of three-components IRM confirm the presence of magnetite, Ti-rich titanomagnetite, and hematite (Fig. 6). A decrease of magnetization just below 575 °C indicates magnetite and a more continuous decrease over larger temperature intervals below 400 °C may be related to Ti-rich titanomagnetite. Because the Curie temperature of Ti-rich titanomagnetite increases during low-temperature oxidation, different oxidation stages within Ti-rich titanomagnetite grains broaden their (un)blocking temperature intervals, which results in a more continuous decrease of IRM intensity. C_{low} can be related to magnetite with some contribution of multi-domain titanomagnetite, and C_{int} to pseudo-single domain or single domain Ti-rich titanomagnetite. A decrease of IRM intensity just below 675 °C in the 2.5 T fraction indicates that C_{high} is residing

Table 1. *Results of cumulative log-Gaussian analysis of IRM acquisition curves; the relation of values within brackets to C_{low} or C_{int} is uncertain*

Specimen	C_{low}		C_{int}		C_{high}		S-ratio
	%	$B_{1/2}$ (mT)	%	$B_{1/2}$ (mT)	%	$B_{1/2}$ (mT)	
abv 1-12-1	–	–	(72	100)	28	562	0.45
abv 6-6-1	40	35	60	88	–	–	0.95
abv 8-3-2	–	–	(79	72)	21	384	0.69
abv 12-2-1	(100	43)	–	–	–	–	1
abv 14-7-1	(45	69)	–	–	55	752	0.08
abv 15-10-1	(79	54)	–	–	21	730	0.69
abv 19-9-1	(70	42)	–	–	30	703	0.54
abv 20-9-1	(100	55)	–	–	–	–	0.99
abv 23-10-1	21	56	79	102	–	–	0.94
abv 25-3-1	52	60	48	91	–	–	0.99
abv 27-10-2	(50	67)	–	–	50	646	0.26
abv 28-8-1	(98	32)	–	–	2	575	0.97
abv 29-4-1	13	29	87	85	–	–	0.98
abv 31-8-1	59	55	41	96	–	–	0.87
abv 35-5-2	–	–	(91	100)	9	631	0.65

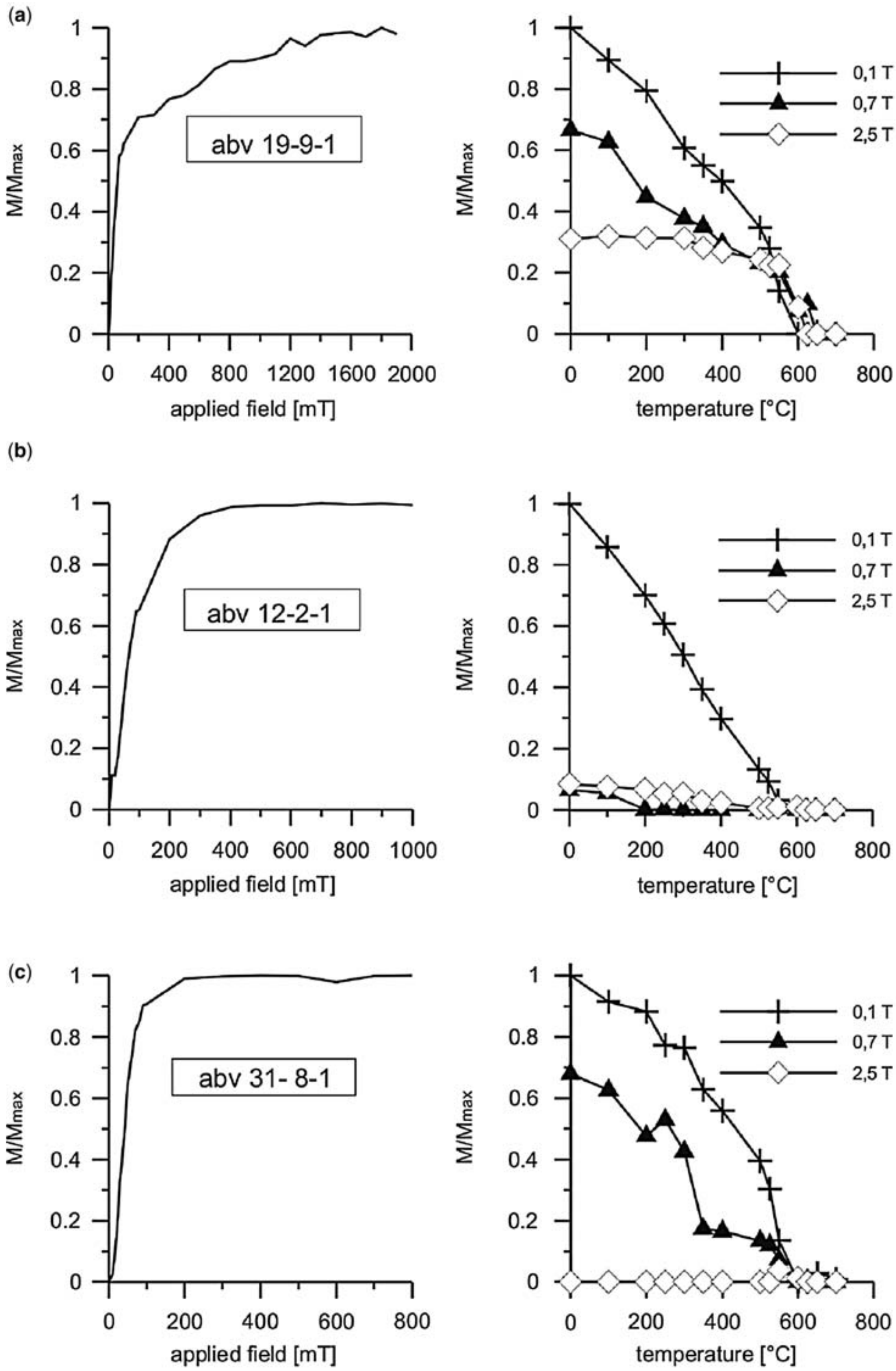

Fig. 6. IRM acquisition curves and thermal demagnetization of three-components IRM of (**a**) abv 19–9–1 (strong hematite contribution), (**b**) abv 12–2–1, and (**c**) abv 31–8-1 (predominant contribution of magnetite and Ti-rich titanomagnetite).

in hematite (Fig. 6a). Contribution of different components to IRM varies considerably between single specimens. About half of the samples contain dominantly magnetically softer components without a detectable content of hematite. Different contribution of C_{int} to the NRM within these specimens is displayed by the S-ratio ($IRM_{-0.3T}/SIRM$), which ranges from 0.865–0.997. Saturation is reached between about 200 and 500 mT. Because of its high spontaneous magnetization M_s, the coercive force of magnetite is shape dominated and has a theoretical maximum of about 300 mT for the saturation field (for indefinite long needles). Therefore saturation fields higher than 300 mT are an indication for the presence of Ti-rich titanomagnetite. Ti-rich titanomagnetites with a composition around $Fe_{2.4}Ti_{0.6}O_4$, typical for basalt, are dominated by stress anisotropy and the coercivity can be increased well above 300 mT by internal stresses (Appel 1987). For the remaining samples lower S-ratios (<0.7) and a significant contribution of C_{high} to the IRM was observed. Saturation fields of these samples have values 1 T which verifies a considerable contribution of hematite (Table 1). For samples with significant content of hematite (C_{high}) only one lower coercive component can be analysed by CLG distribution, and its relation to C_{low} or C_{int} is uncertain because of limited resolution.

Figure 7 displays bivariate plots of NRM and SIRM v. magnetic susceptibility κ. The parameters show high variations between single sites. NRM values are very low for basalts which could be an indication for strong alteration and therefore a secondary origin of the NRM. A positive relationship between κ and NRM or SIRM is given for SIRM values above about 5×10^3 mA m^{-1} and NRM values above about 50 mA m^{-1}. This indicates very different concentrations of ferro(i)magnetic minerals. A complex nature of NRM is furthermore supported by a strong variation of NRM/SIRM ratios.

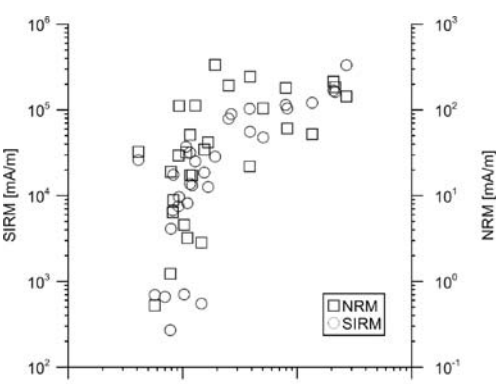

Fig. 7. Bivariate plots of NRM and SIRM v. magnetic susceptibility.

Palaeomagnetic results

Remanence directions were determined from straight segments in the Zijderveld-diagram using principal component analyses. For the component with highest coercivity also stable end point directions were used. The demagnetization behaviour within single sites was mainly smooth and easy to analyse; directions of characteristic components in general show good grouping (Fig. 8). In contrast, site mean directions obtained by Fisher statistics (Fisher 1953) vary to a high extent. Basically AfD of NRM shows three different components (Fig. 9): a low-coercivity component (LC-C) which is demagnetized at field intervals between 0 and 20 mT, a high-coercivity component (HC-C) demagnetized at fields between 15 and 100 mT, and an ultra-high coercivity component (UC-C) defined as the direction remaining at 100 mT. In accordance with results of rock magnetic investigations, we relate the LC-C to magnetite with a possible contribution of multi-domain titanomagnetite, the HC-C to Ti-rich titanomagnetite, and the UC-C to hematite. Relative contribution of different components to NRM varies to a high extent between single sites. In most sites, the HC-C represents the highest contribution (Fig. 9a). To a minor degree, the LC-C or UC-C are more dominant (Fig. 9b, c). All components show partly normal and reverse directions. For statistical analysis, reverse polarity directions were inverted.

ThD of NRM applied to sites with more than about 75% of magnetization left after AfD reveals a high-temperature component (HT-C) unblocking in the range of 500–580 °C and an ultra-high temperature component (UT-C) unblocking above 600 °C (Fig. 10a). These components are most

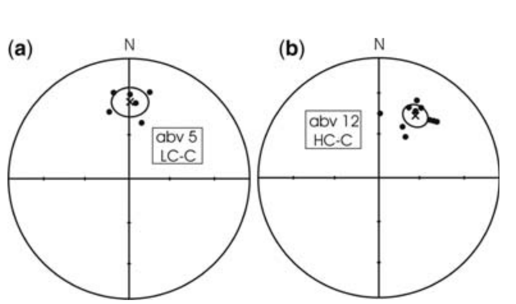

Fig. 8. Equal area stereoplots of single sites (geographical coordinates): (**a**) LC-C of abv 5; (**b**) HC-C of abv 12. Black cross, mean direction; black circle, 95% confidence limit.

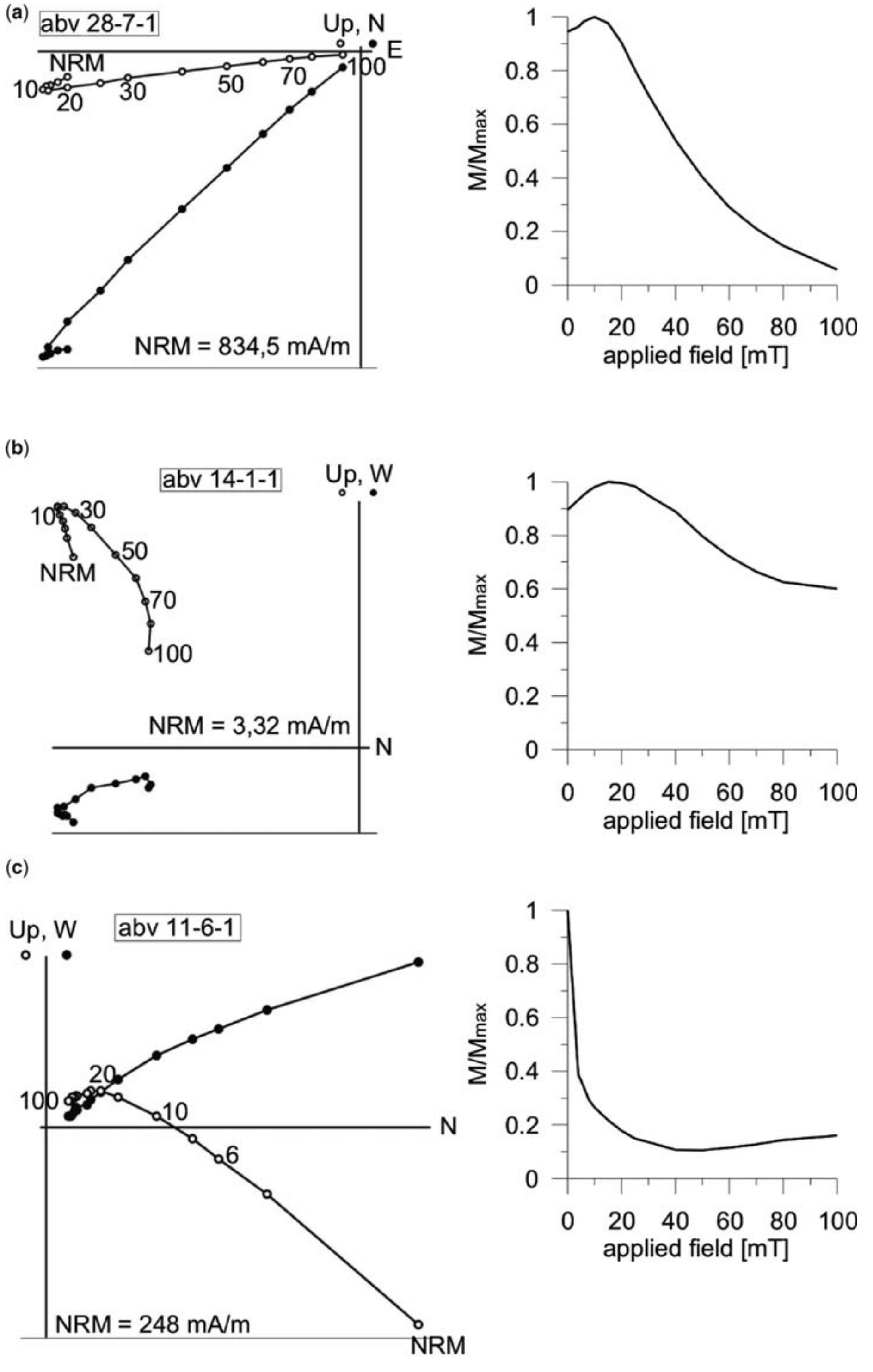

Fig. 9. Zijderveld-diagrams and intensity curves of alternating field demagnetization for representative samples (geographical coordinates): (**a**) abv 28-7-1; (**b**) abv 14-1-1; (**c**) abv 11-6-1.

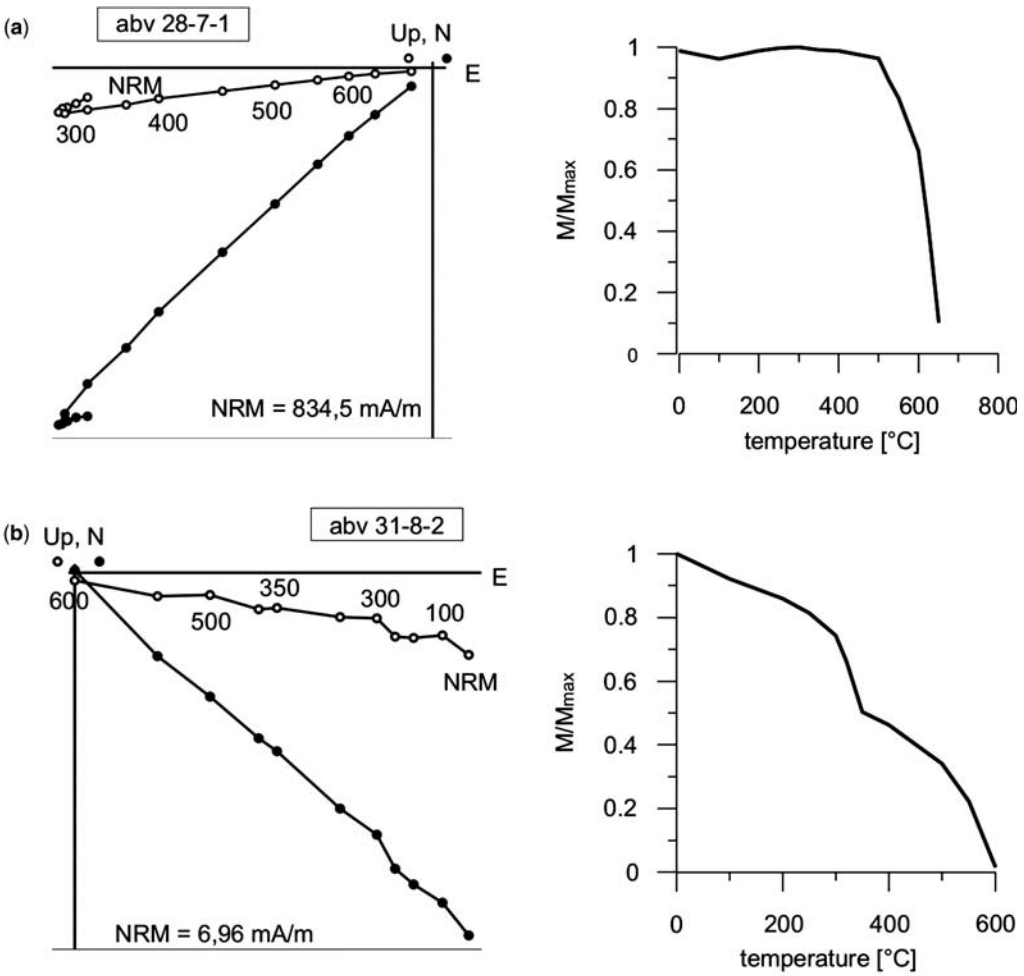

Fig. 10. Zijderveld-diagrams and intensity curves of thermal demagnetization for representative samples (geographical coordinates): (**a**) abv 28-7-1; (**b**) abv 31-8-2.

likely related to magnetite and hematite, respectively. In few specimens also a low-temperature component (LT-C) demagnetized below 450 °C occurs, which can be allocated to Ti-rich titanomagnetite (Fig. 10b). Comparison of AfD and ThD reveals coincidence of the UC-C and UT-C, which confirms that both are related to hematite. No distinct correlation of other components was found. In addition, three sites showing significant results by AfD were thermally demagnetized to obtain further relationships between components. Most specimens of these sites reveal a high increase in magnetization between 500 and 625 °C, probably indicating new formation of magnetite due to high temperature oxidation of Ti-rich titanomagnetite. This is confirmed by a strong increase in magnetic susceptibility at the same temperatures. Unfortunately remanence directions of the newly formed magnetite obscure directions of initial (titano)magnetite and therefore no characteristic remanence directions could be isolated.

Site mean directions and statistical parameters are listed in Table 2. AMS measurements were done in order to exclude that remanence directions were significantly influenced by magnetic anisotropy. A generally low degree with P-factors (Jelinek 1977) ranging from 1.007–1.031, and a random distribution of the principle susceptibility axes confirm a low influence of magnetic anisotropy. Site mean values of the UC-C show a rather random distribution and therefore are not further discussed. Figure 11 shows equal area stereoplots

Table 2. *Site mean directions and statistical parameters of LC-C and HC-C*

Site	lat. (°N)	long. (°E)	C	N_m	N_i (nor./rev.)	Bedding dip dir./dip	*In situ* Dec. (°)	Inc. (°)	Tilt corrected Dec. (°)	Inc. (°)	α_{95}	k
abv 1	28°19.776′	94°58.116′	LC-C	9	5 (5/0)	–	26.1	49.6	–	–	10.4	55.1
			HC-C	9	7 (5/2)	–	43.1	10	–	–	24.7	7.1
abv 2	28°19.206′	94°59.323′	LC-C	8	7 (7/0)	–	160.2	−51.4	–	–	43.2	2.9
			HC-C	8	6 (6/0)	–	1.7	42.3	–	–	8.5	62.7
abv 3	28°19.388′	94°59.621′	LC-C	9	7 (4/3)	–	135.6	−33.3	–	–	37	3.6
			HC-C	9	8 (8/0)	–	68	26.4	–	–	11.9	22.6
abv 4	28°20.556′	94°59.392′	LC-C	8	5 (5/0)	–	340.8	57.5	–	–	45.8	3.7
			HC-C	8	6 (6/0)	–	351	84.6	–	–	22	10.2
abv 5	28°20.822′	95°00.183′	LC-C	8	6 (6/0)	–	0.7	36.3	–	–	11.1	37.3
			HC-C	8	8 (8/0)	–	89.1	32.8	–	–	13.2	18.5
abv 6	28°20.858′	95°00.497′	LC-C	9	5 (2/3)	–	65.7	23.8	–	–	18.4	18.2
			HC-C	9	7 (7/0)	–	109.9	33.5	–	–	7.5	65
abv 8	28°23.299′	95°04.665′	LC-C	9	5 (4/1)	–	296.2	−26.6	–	–	41.3	4.4
			HC-C	8	7 (6/1)	–	126.7	31.2	–	–	4.3	193.7
abv 9	28°23.030′	95°04.513′	LC-C	8	5 (0/5)	–	102.5	12.1	–	–	21.7	19
			HC-C	8	8 (8/0)	–	90	15.5	–	–	11.9	22.7
abv 11	28°21.172′	95°02.834′	LC-C	10	10 (10/0)	–	357.3	36.3	–	–	13.6	13.5
			HC-C	10	8 (0/8)	–	140.2	36.5	–	–	16.3	12.5
abv 12	28°44.687′	94°52.792′	LC-C	10	3 (3/0)	–	107.1	−22.7	–	–	49.4	7.3
			HC-C	10	10 (10/0)	–	30.4	39.8	–	–	8	37.6
abv 13	28°43.844′	94°55.432′	LC-C	8	7 (7/0)	100/45	24.8	19.4	34	3.7	45.4	2.7
			HC-C	8	8 (3/5)	–	135.1	9.4	139.6	−27.1	22.4	7.1
abv 14	28°43.050′	94°57.448′	LC-C	8	8 (6/2)	–	14	46.5	–	–	30.8	4.2
			HC-C	8	8 (2/6)	–	355.5	41.8	–	–	18	9.2
abv 15	28°42.641′	94°57.903′	LC-C	8	5 (5/0)	–	352.9	−44.2	–	–	61.9	2.5
			HC-C	8	4 (3/1)	–	329.3	26.3	–	–	5.2	309.6
abv 18	28°22.518′	95°03.854′	LC-C	8	8 (5/3)	–	355	25.3	–	–	39.8	2.4
			HC-C	8	8 (5/3)	–	266.8	-9.4	–	–	30.5	3.8
abv 19	28°22.353′	95°03.773′	LC-C	9	3 (0/3)	–	109.8	7.3	–	–	89.3	3
			HC-C	9	6 (6/0)	–	220.6	46.9	–	–	6.6	104.1
abv 20	28°21.083′	95°02.854′	HC-C	9	9 (0/9)	077/21	155.9	75.5	109.1	62.4	2.2	532.8
abv 21	28°21.083′	95°02.854′	LC-C	8	7 (2/5)	078/22	327.4	68.3	21.3	65.5	29.8	5
			HC-C	8	8 (7/1)		207.5	65.1	152.3	70.3	13.3	18.3
abv 22	28°21.083′	95°02.854′	LC-C	8	5 (5/0)	015/40	55.6	71.6	29.5	34.9	14.8	27.8
			HC-C	8	8 (0/8)		33.8	69.2	22.6	30	9.2	37.5

(*Continued*)

Table 2. *Continued*

Site	lat. (°N)	long. (°E)	C	N_m	N_i (nor./rev.)	Bedding dip dir./dip	*In situ* Dec. (°)	Inc. (°)	Tilt corrected Dec. (°)	Inc. (°)	α_{95}	k
abv 23	28°25.699′	95°15.882′	LC-C	8	4 (4/0)	110/18	22.2	61.6	51.3	56.2	7.9	34.9
			HC-C	8	7 (7/0)	–	49.5	74.2	80.8	60.9	17.7	12.6
abv 24	28°25.434′	95°15.666′	–			–			–	–		
abv 25	28°25.245′	95°14.652′	LC-C	8	8 (5/3)	–	48.8	22.8	–	–	27.6	5
			HC-C	8	8 (8/0)	–	92.3	37.5	–	–	15.6	13.5
abv 26	28°22.889′	95°13.802′	HC-C	10	10 (8/2)	–	253.6	28.3	–	–	20.4	6.6
abv 27	28°21.996′	95°13.294′	HC-C	8	3 (2/1)	–	230.4	− 64	–	–	2.4	108.8
abv 28	28°21.654′	95°13.020′	LC-C	8	7 (6/1)	065/78	61.7	28.9	60.6	−49	26.8	6
			HC-C	8	8 (7/1)	–	216.8	2.6	171.4	60.5	5.6	98.6
abv 29	28°15.693′	95°12.841′	LC-C	10	10 (3/7)	–	74	25.4	–	–	28.3	9.2
			HC-C	10	10 (1/9)	–	338.4	36.3	–	–	29	3.7
abv 30	28°12.273′	95°13.547′	LC-C	8	5 (5/0)	–	205.7	−17.3	–	–	40.5	4.5
			HC-C	8	6 (0/6)	–	282.3	8.5	–	–	4.3	243.2
abv 31	28°10.405′	95°01.320′	LC-C	9	9 (5/4)	220/51	338.7	7.1	333.7	3.5	25	5.2
			HC-C	9	8 (0/8)	–	57.6	20.6	36.3	68.7	7	63.8
abv 32	28°08.448′	96°05.568′	LC-C	9	9 (6/3)	–	53	−0.3	–	–	38.6	2.7
			HC-C	9	9 (3/6)	–	132.2	−11.6	–	–	42.4	2.4
abv 33	28°08.177′	95°06.162′	LC-C	9	9 (9/0)	302/38	264.2	36	272.2	4	35.1	8.8
			HC-C	9	9 (7/2)	–	13.6	8.8	12.1	−4.1	9.1	32.8
abv 34	28°08.083′	95°08.115′	LC-C	8	6 (4/2)	320/18	27.3	24.6	21.1	16.7	16.7	5.3
			HC-C	8	6 (6/0)	–	201.1	11.1	205.5	19.2	5.4	125.8
abv 35	28°08.279′	95°08.725′	HC-C	8	6 (6/0)	–	212.3	82.5	–	–	19.2	13.1
abv 36	28°14.407′	94°59.340′	LC-C	8	8 (7/1)	–	312.8	67.4	–	–	11	26.2
abv 37	28°11.332′	95°00.277′	LC-C	9	9 (9/0)	–	28.6	52	–	–	12.5	17.9
			HC-C	9	8 (4/4)	–	79.9	38.4	–	–	10.3	29.6
abv 38	28°09.087′	94°03.872′	LC-C	10	4 (4/0)	–	354.5	76.5	–	–	32.2	9.1
			HC-C	10	10 (10/0)	–	50.1	62.6	–	–	8	377.9
abv 39	28°12.728′	94°14.055′	–			–			–	–		

lat., latitude; long., longitude; N_m, number of specimens measured; N_i, number of specimens included in statistics; nor., normal polarity; rev., reverse polarity; dip dir., dip direction; Dec., declination; Inc., inclination; $\alpha95$, 95% confidence angle; k, precision parameter; missing site numbers are due to sampled pilot sites of the Yinkiong formation; the bedding was obtained by adjacent sediments.

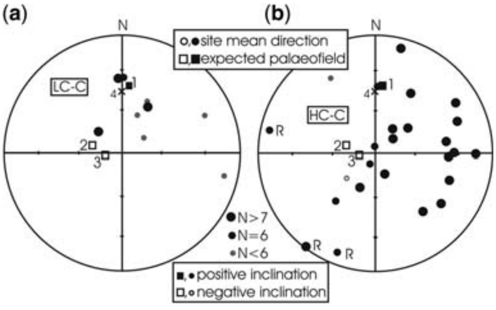

Fig. 11. Equal area stereoplots of site mean directions (geographical coordinates) for the (**a**) LC-C and (**b**) HC-C. Only sites with k > 10 and α_{95} < 25 are displayed. Expected palaeodirections for the study area for Early Miocene (no. 1), Early Permian (no. 2), and Upper Carboniferous (no. 3) are also shown (calculated from the APWP of Besse & Courtillot (2002) for 1 and McFadden & McElhinny (1995) for 2&3), as well as the present day Earth's magnetic dipole field (no. 4). Directions marked by 'R' were inverted in Figure 12 (a). N, number of specimens.

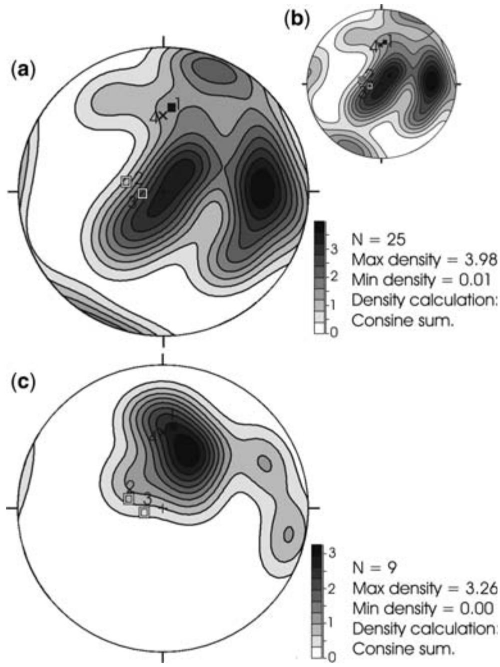

Fig. 12. Density plots of site mean directions in geographical coordinates (lower hemisphere) of (**a**) HC-C (inverted directions: abv 28, abv 30, abv 34; see Fig. 11b); (**b**) HC-C without inverted directions; (**c**) LC-C. Numbers of expected palaeofields and the present day Earth's magnetic field are explained in Figure 11. Only sites with k > 10 and α_{95} < 25 were used.

of remanence directions residing in the LC-C and HC-C, as well as expected palaeodirections for possible remanence acquisition ages and the present day Earth's magnetic dipole field. In Figure 11 density plots of the LC-C and HC-C are displayed. In the case of the LC-C a trend of north-pointing directions with inclinations slightly higher than the present day Earth's magnetic dipole field (46.8°) occurs. The HC-C yields a trend to clockwise rotations and a second trend of very steep inclinations (>60°) which fits to the expected palaeofields of Upper Carboniferous–Early Permian (Fig. 12b). Few sites of the LC-C also show inclinations >60°.

Bedding data could be obtained only at site locations where the contact between volcanic rocks and sediments was exposed, that is, at nine sites. Because of the complex structure of the area and insufficient structural data, results of fold tests are ambiguous. The McFadden (1990) fold test and the inclination-only fold test (Enkin & Watson 1996) were applied to the HC-C and the LC-C of all sites with structural control, separated for components with higher inclinations (sites abv 20–23) and lower inclinations (sites abv 13, abv 28, abv 31, abv 33, abv 34). In all cases the McFadden (1990) fold test did not reach the 95% significance level. The inclination-only fold test was used to exclude effects due to different vertical axis rotations. Determination of the k-value was performed after Enkin & Watson (1996), whose method is also applicable to steep inclinations. Results for the sites with lower inclinations and with higher inclinations are similar and support a secondary origin of both the LC-C and the HC-C (Fig. 13).

Geochronology and thermochronology

The geochronology of basaltic lithologies is difficult, due to the typically low abundance of radiogenic elements and the chemical instability of the datable phases such as plagioclase, mafic silicates and glass. The collected pilot samples are typically fine grained, hampering the separation of pure mineral phases. We have performed whole rock K–Ar geochronology on five basalt samples and additionally on one shale sample from the Yinkiong Fm. A relatively fresh large basalt boulder from a river bed in the Changsin valley north of the Siang river towards Sibbum was dated to Late Carboniferous age (319 ± 15 Ma). Further basaltic samples yield ages between 87.2 ± 1.3 and 24.9 ± 0.4 Ma. Fine mineral fractions (<2 μm and <0.2 μm) of the shale sample yielded 62.3 ± 0.7 and 46.8 ± 0.7 Ma, respectively (see analytical details in Table 3).

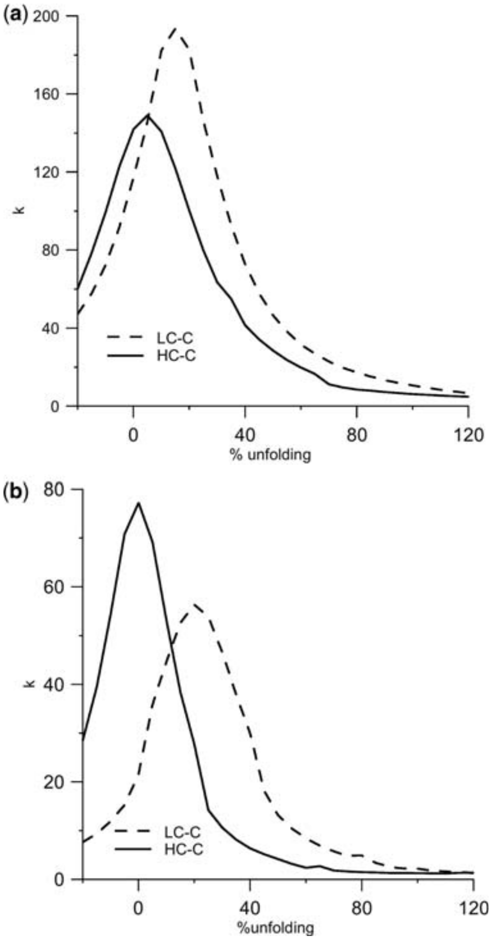

Fig. 13. Results of the inclination-only fold tests (Enkin & Watson 1996) for: (**a**) all sites with higher inclinations; and (**b**) all sites with lower inclinations.

Zircon fission track (ZFT) and (U–Th)/He (ZHe) low-temperature thermochronology were performed on two grey quartz wacke samples of the Yinkiong Fm and on a quartzite sample of the Miri Fm, in order to constrain the provenance signatures and the post-effusive thermal history of the Siang window. In each case, ZFT and ZHe analyses were performed on zircon aliquots from the same sample. The results of ZFT age determinations are listed in Table 3. The single grain ages show a wide scatter; the chi-square tests fail and the values of dispersion are also high. The central ages calculated for the samples have therefore no any geological meaning. In the samples the single grain ages form relatively distinct clusters around 150 and 260 Ma (AbV-11b), 70 and 260 Ma (YS-7) and *c.* 56 Ma (YS-16a) indicating the mixed character of the samples (Fig. 14). The zircon (U–Th)/He ages range between 71 and 9 Ma; they are considerably younger than the ZFT ages.

Discussion

Age constraints on the Abor volcanism and deposition of the sediments

Due to the dense vegetation the contact between sedimentary rocks and Abor volcanic rocks is rarely exposed, which makes it difficult to determine the stratigraphic position of the volcanic rocks. Intercalation of the Abor volcanic rocks with the sediments of the Yinkiong Fm, as described by Jain & Thakur (1978), Singh & Kumar (1990), Singh (1993), and Acharyya (2007) was not observed within the sampling area, thus our geochronological results cannot directly constrain the Late Paleocene to Early Eocene age of the Abor volcanism (cf. Acharyya 1994). One basalt sample yields a Late Carboniferous whole rock K–Ar age (319 ± 15 Ma), which, within analytical uncertainty, agrees with the biostratigraphic age assignment based on mollusc and palaeofloral assemblages (Singh 1981; Sinha *et al.* 1986). This age datum provides the first geochronological support for Late Palaeozoic volcanism in the Siang Valley. Other basalt samples yield K–Ar ages between 87.2 ± 1.3 and 24.9 ± 0.4 Ma. These results are interpreted as partly reset ages resulting from argon loss during the partial transformation of the sampled volcanic rocks. This process is reflected also in the formation of epidote and chlorite in the feldspars and the glassy matrix of some samples. In addition, rock magnetic analyses reveal advanced low-temperature oxidation of Ti-rich titanomagnetite. Finally, major element geochemical patterns also indicate a post-effusive oxidation (Sengupta *et al.* 1996).

According to the low-temperature chronometers the transformation of the rock-forming phases and the oxidation of the Fe-oxides took place under diagenetic conditions. Zircon fission track ages form well defined age clusters. The individual zircon grains in the age clusters have similar uranium content, thus the metamictization-controlled partial rejuvenation of the young populations is not probable. We interpret the age clusters as Permian, Jurassic, Late Cretaceous, and Paleocene cooling or formation ages of the zircon-bearing rocks of the source area of the sediment (Fig. 14). The temperature range of ZFT partial reset is around 220–260 °C; the ZFT age distribution of the sandstone samples clearly show that during their thermal evolution they remained below this threshold. The young age clusters of the Yinkiong

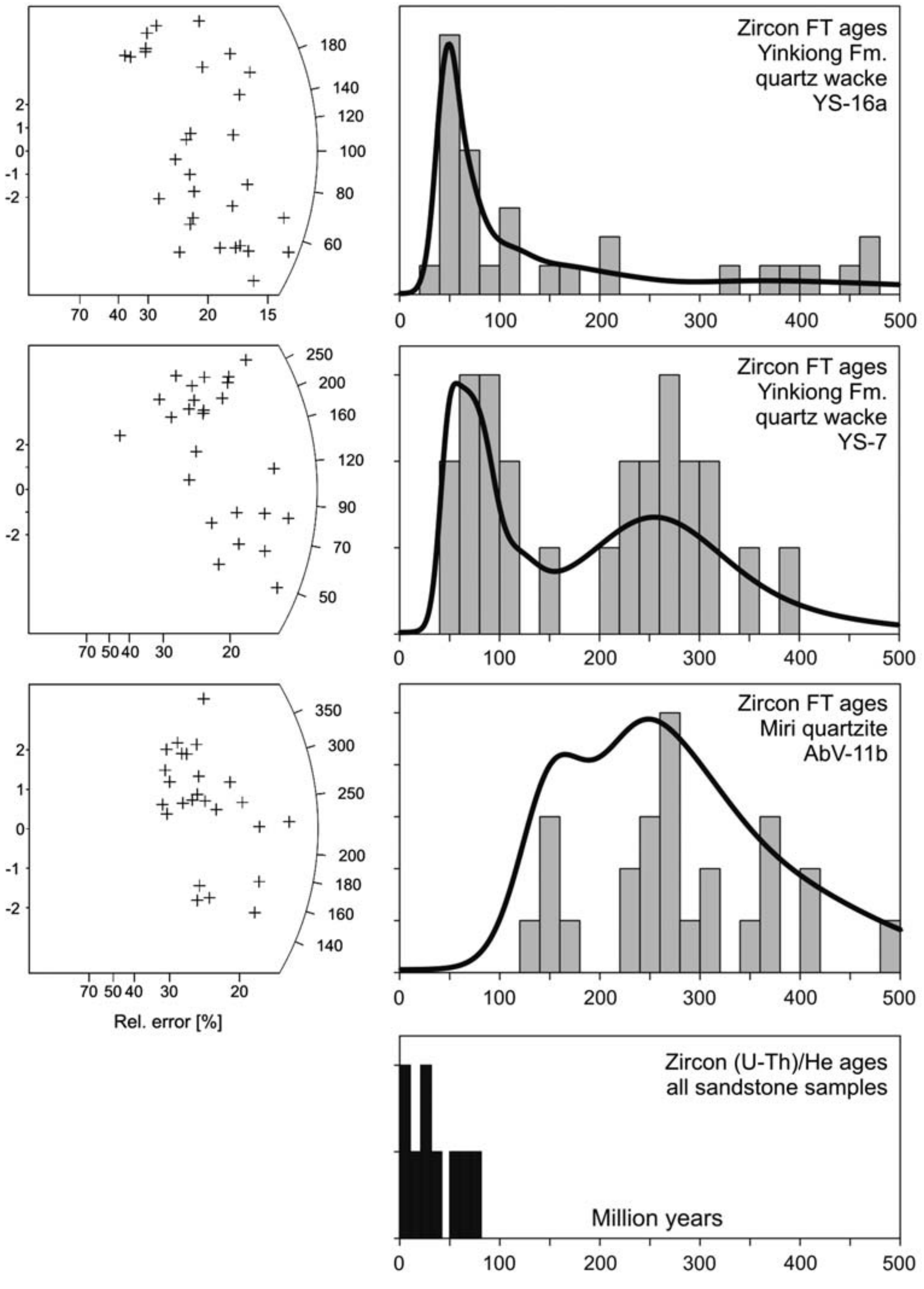

Fig. 14. Zircon fission track and (U–Th)/He single grain age distributions of the sandstone samples.

Fm samples preclude the sedimentation age of the sandstones being Permian, and documents that their deposition occurred after *c*. 56 Ma. The youngest age cluster of the Miri Quartzite at *c*. 150 Ma does not support the widely suggested Proterozoic to Permian ages for this unit. Very probably, the major source of both the Yinkiong and Miri sediments was located on the overriding Asian plate

Table 3a. *Results from geochronology: (a) K–Ar dating of the basalts and shales*

Sample	Lithology	K_2O (wt. %)	$^{40}Ar^*$ (nl/g) STP	$^{40}Ar^*$ (%)	Age (Ma)	2 s-Error (Ma)
Drift boulder	Hyaloclastic basalt	0.11	1.24	30.62	319.4	14.8
AbV-1	Basalt	0.49	1.411	72.56	87.2	1.3
AbV-14	Basalt	0.93	1.540	70.64	50.6	0.7
AbV-20	Basalt	1.88	1.522	67.29	24.9	0.4
AbV-24	Basalt	2.01	1.693	37.12	25.9	0.7
YS 10b <2 μm	Shale	3.50	7.150	86.82	62.3	0.7
YS 10b <0.2 μm	Shale	3.80	5.810	81.10	46.8	0.7

Samples used for geochronology are indicated by 'AbV' or 'YS' to distinguish them from samples used for palaeomagnetic analyses ('abv'). Sample numbers indicate the sampling site, the site locations of the AbV samples are given in Table 2. Locations of the YS sites are adjacent to AbV-8 (YS 7) and AbV-11 (YS 10). No volcanic rocks are exposed near site YS 16 in the Sirnyuk Valley at Jegging (28°31.578′N/95°02.970′E). The drift boulder was located at 28°18′N/95°11′E.

and/or in the Gangdese thrust belt; the Jurassic to Cretaceous thermal events retained in the detrital zircon age spectra can clearly not be connected to the Indian Plate. The Yinkiong Fm underwent burial soon after its deposition as indicated by the *c*. 47 Ma K–Ar age of the shale in its 0.2 μm size fraction – the age of diagenetic illite growth – from which the youngest detrital ZFT age clusters do not differ significantly. Our results infer that volcanic bodies intruding the Miri quartzites or interbedded with the Yinkiong Fm are clearly post-Permian, and pertain to a volcanism latest Cretaceous to Early Tertiary in age. We therefore conclude that the Siang window exposes the products of more than one major volcanic event, which confirms the model put forward earlier by Singh (1984), Singh & De (1984) and Singh & Malhotra (1987).

Age of remanence acquisition

The single crystal zircon (U–Th)/He ages show an extremely wide scatter between latest Cretaceous and Late Miocene (Table 3b). A part of the ZHe ages are considerably younger than the youngest age cluster in the ZFT ages and even younger than the base of the Siwalik Group below the MBT. Thus, the ZHe ages cannot be cooling ages of the source terrains of the sediment; the ZHe thermochronometer underwent partial degassing after the sedimentation. This process results in a wide scatter in ages, because the diffusion of He (and thus the closure temperature) depends on the size, shape, content of U & Th, and their distribution, as well as alpha dosage of the individual crystals. Reiners *et al.* (2004) determined the closure temperature of the ZHe thermochronometer to be *c*. 180 °C. The dated samples were close to this threshold, but definitely below it. From the distribution of the ZHe ages, from the size of the dated zircon crystals, as well as based on the agreement of the Cenozoic K–Ar ages between basalt and shale samples we postulate that the Siang window rocks (Miri Fm. Abor volcanic series, Yinkiong Fm.) shared a largely common thermal history since Palaeogene times and experienced a maximum burial temperature around 150–170 °C for the Late Miocene time.

Applied fold tests (McFadden 1990; Enkin & Watson 1996) suggest a secondary formation of both the LC-C and the HC-C. The occurrence of Ti-rich titanomagnetite constrains the possible peak temperature of metamorphism to ≤350 °C as at higher temperatures Ti-rich titanomagnetite would have decayed into magnetite and ilmentite near phases (Grommé *et al.* 1969; Tucker & O'Reilly 1980). Few studies of the metamorphic evolution of adjacent areas were made. Goswami *et al.* (2009) report results of structural and metamorphic analyses on rocks of the Lesser and Greater Himalayan sequences in the western Arunachal Himalaya and Gururajan & Chowdhury (2003) report a low-grade metamorphic event in the Lesser Himalaya of the Lohit valley located south-east of the Siang window. In both cases timing is poorly constrained. Ding *et al.* (2001) report high grade metamorphic events in the Namche Barwa Syntaxis at about 160, 65, 40, and 11 Ma. According to Booth *et al.* (2009) the Namula thrust separates high-grade rocks at the core of the Namche Barwa Syntaxis to the north from lower grade rocks to the south. The younger K–Ar ages of the present study (87.2–24.9 Ma) are very likely partly reset ages and reveal an overprinting event which occurred probably between the India–Asia collision and Early Miocene. This would fit to high-grade metamorphism in the Namche Barwa Syntaxis at 40 Ma, which is related to the early stages of the India–Asia collision (Ding *et al.* 2001). In addition, Dunkl *et al.* (2007) reported a metamorphic event at *c*. 24 Ma in the Triassic flysch of the Tethyan Himalayan in SE Tibet, which also fits to the

Table 3b. *Zircon(U–Th)/He data*

Sample	aliq.	He vol. (ncc)	He s.e. (ncc)	U238 mass (ng)	U238 s.e. (ng)	Th232 mass (ng)	Th232 s.e. (ng)	Th/U ratio	Sm mass (ng)	Sm s.e. (ng)	Ejection correct. (Ft)	Uncor. He-age (Ma)	Ft–Cor. He-age (Ma)	1 s (Ma)
YS 16a	#1	**1.534**	0.026	0.861	0.016	0.258	0.006	0.30	0.014	0.001	0.71	*13.8*	**19.5**	0.5
	#2	**2.087**	0.036	0.650	0.012	0.198	0.005	0.30	0.011	0.001	0.74	*24.8*	**33.4**	0.8
	#3	**0.813**	0.015	0.812	0.015	0.536	0.013	0.66	0.051	0.003	0.74	*7.2*	**9.7**	0.2
AbV-11b	#1	**5.163**	0.086	0.851	0.015	0.340	0.008	0.40	0.016	0.001	0.74	*45.8*	**61.6**	1.4
	#2	**5.662**	0.094	1.009	0.018	0.677	0.016	0.67	0.029	0.002	0.76	*40.0*	**52.9**	1.2
	#3	**2.096**	0.036	0.761	0.014	0.876	0.021	1.15	0.020	0.001	0.75	*17.9*	**23.9**	0.5
YS 7	#1	**0.308**	0.006	0.322	0.006	0.241	0.006	0.75	0.041	0.003	0.69	*6.7*	**9.8**	0.2
	#2	**1.092**	0.019	0.571	0.010	0.192	0.005	0.34	0.005	0.000	0.67	*14.7*	**21.8**	0.5
	#3	**5.328**	0.089	0.761	0.014	0.825	0.020	1.08	0.021	0.001	0.64	*46.0*	**71.4**	1.6

Numbers in italics: rough uncorrected data.
Numbers in bold: age, which can be interpreted in context with geological evolution.

Table 3c. *Zircon fission track results obtained on the sandstone samples from Arunachal*

Sample	Crystal	RhoS	(Ns)	RhoI	(Ni)	RhoD	(Nd)	Chi-sq. P (%)	Disp.	Central Age	±	1 s
YS-16a	30	80.2	(2595)	39.5	(1276)	7.97	(4200)	0	0.70	100	±	13
YS-7	25	123.8	(2446)	41.8	(826)	7.94	(4200)	0	0.65	144	±	20
AbV-11b	25	150.2	(2687)	30.7	(550)	8.39	(4200)	0	0.25	256	±	19

Track densities (RHO) are as measured ($\times 10^5$ tr/cm^2); number of tracks counted (N) are shown in brackets. RhoD and Nd are track densities and number of tracks in the CN2 detector. Chi-sq P(%): probability obtaining Chi-square value for *n* degrees of freedom (where $n =$ no. crystals-1). Disp., dispersion, according to Galbraith & Laslett (1993). Central ages calculated using dosimeter glass: CN 2.

possible timing of metamorphic overprint within the Siang window. Our new geochronological results suggest that the regional thermal overprint in the Siang window did not exceed the diagenetic stage.

The clockwise rotation trends of the HC-C would fit to a clockwise rotation trend reported from palaeomagnetic investigations on Cretaceous to Miocene rocks north and east of the Namche Barwa Syntaxis (Fig. 15 and Table 4; Otofuji *et al.*

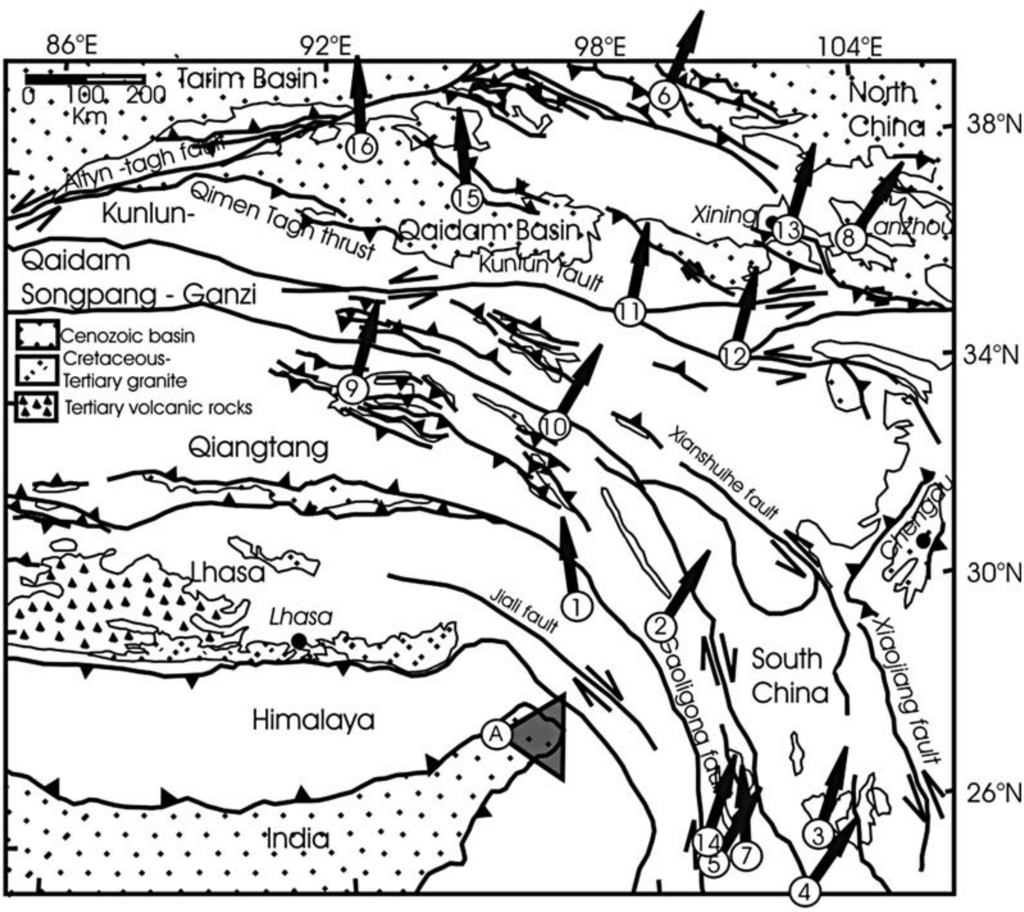

Fig. 15. Map of the eastern part of the Himalayas (modified after Dupont-Nivet *et al.* 2002) showing the declination maximum (HC-C; density >2.3) of the Abor volcanic rocks (grey area marked by 'A'). Additionally, rotations with respect to stable Eurasia are displayed by the black arrows marked with numbers. The rotations were determined by the difference between expected declinations (APWP of Eurasia; Besse & Courtillot 2002) and observed declinations of previous palaeomagnetic studies; references are given in Table 4.

Table 4. *Results of previous palaeomagnetic investigations on the eastern Tibetan Plateau*

No.	locality	lat. (°N)	long. (°E)	Age	D_o	D_e	D_{rot} ($D_o - D_e$)	α_{95}	ref.
1	Yàan	30.1	103	Cr	2.1	10.1	−8	11.3	1
2	Markam	29.7	98.6	lCr	48.2	16	32.2	8.8	1
3	Yuanmou	25.9	101.7	uCr	26.9	9.6	17.3	3.6	2
4	Chuxiong	25	101.5	Cr	44.6	9.7	34.9	10.7	3
5	Yongping	25.5	99.5	lCr	42	10.5	31.5	15.7	4
6	Hekou group	39	99.6	lCr	41.9	16.9	24	5.1	5
7	Lanping Basin	25.6	100.5	uCr	6.9	9.5	−2.6	8.6	6
8	Xining – lanzhou	36.2	103.5	lCr	44.7	10.7	34	5.1	7
9	Fenghuoshan	34.5	92.8	Ec	25.5	9.6	15.9	6	8
10	Yushu	33.2	96.7	Mi	35.6	5.3	30.3	9	9
11	Tuoluo	35.3	98.6	Mi	20.1	8.8	11.3	27.1	9
12	Jungong	34.7	100.7	Mi	19.8	5.2	14.6	6	9
13	Xining	36.5	102	Ec	29.3	12.8	16.5	13.2	9
14	Lanping Basin	25.8	99.4	uCr	28.1	9.5	18.6	2.4	10
15	Xiao Qaidam (HTC)	37.4	95.3	Mi	0.7	5.7	−5	5.8	11
16	E Bo Liang	38.7	92.8	Og	8	10.6	−2.6	5.1	11

lat., latitude; long., longitude; D, declination; o, observed; e, expected; rot, rotation; α_{95}, 95% confidence limit; ref., reference; Mi, Miocene; Og, Oligocene; Ec, Eocene; Cr, Cretaceous; l, lower; u, upper.
References: 1: Otofuji *et al.* (1990), 2: Otofuji *et al.* (1998), 3: Funahara *et al.* (1992), 4: Funahara *et al.* (1993), 5: Huang *et al.* (1992), 6: Huang & Opdyke (1993), 7: Halim *et al.* (1998), 8: Halim *et al.* (1998) and Lin & Watts (1988), 9: Cogné *et al.* (1999), 10: Yang *et al.* (2001), 11: Dupont-Nivet *et al.* (2002).

1990, 1998; Funahara *et al.* 1992, 1993; Huang & Opdyke 1993; Sato *et al.* 1999, 2007; Yang *et al.* 2001). The LC-C shows a trend of remanence directions which are close to the present day Earth's magnetic dipole field. These directions indicate a more recent component probably formed during alteration of the rocks. The trend to high inclinations (>60°) of the HC-C could be due to: (a) tilting around horizontal axis after remanence acquisition; or (b) a primary remanent magnetization of Late Palaeozoic age. Remanence directions residing in HC-C are plotted in Figure 16 on a structural map of the Siang window. The sites with high inclinations are marked by orange circles. No clear correlation to structures on the map can be identified. However, six of the sites with high inclinations (abv 4, abv 20, abv 21, abv 22, abv 35, abv 38) can be connected by an approximately NNW–SSE trending line, which is the general trend of most fold axis and faults. Whether this is an indication for a larger structure (i.e., the axis of the anticline of the Siang window) is questionable as it is difficult to explain why adjacent sites (with lower inclinations) should not have been tilted in the same way. Steepening of the inclinations could rather be due to small scale local tilting of the rocks. A possible explanation could be a system of duplex structures, as it is common in the Lesser Himalaya and the Siwaliks (e.g. Srivastava & Mitra 1994; DeCelles *et al.* 2001). The second possibility would be a primary magnetization with a Late Palaeozoic remanence age. Expected Late Palaeozoic palaeodirections yield inclinations between −69° and −78° (Fig. 11). Therefore a primary magnetization acquired during emplacement of the Abor volcanic rocks at Late Palaeozoic could explain the high inclinations. However, applied fold tests indicate a secondary origin of remanent magnetization for the high-inclination sites; results of the fold tests are based on four sites with high inclinations only and should be regarded with caution. The Siang window was affected by several deformation events (Jain & Tandon 1974; Singh 1993; Kumar 1997) and the sites are clearly not positioned on two different limbs of one single fold as would be the ideal case for a fold test. Therefore a primary magnetization of the high inclination sites cannot completely be ruled out. Similar rock magnetic properties of the sites with low and high inclinations are not supportive for a partly primary origin. Clarifying the origin of the high-inclination sites is not possible within the present study and calls for further structural and palaeomagnetic investigations.

Structural implications and clockwise rotation

Figure 16 demonstrates that the complex pattern of remanence directions is probably due to strong tectonic deformation of the area. The partly high variation in declination and/or inclination of nearby sites indicates small scale structural deformation.

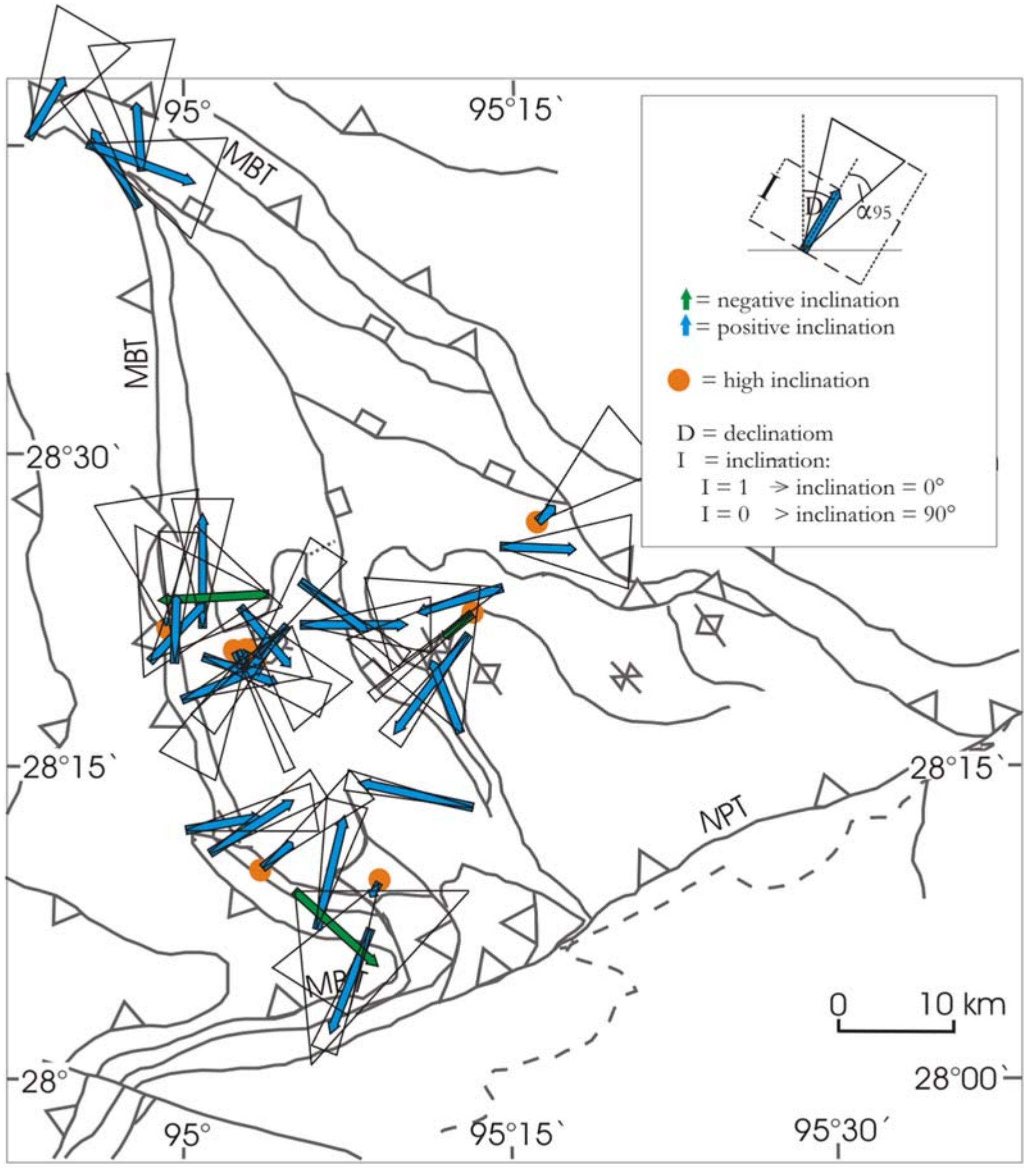

Fig. 16. Structural map of the Siang window (modified after Acharyya & Saha 2008) displaying observed declinations, inclinations, and values of α_{95} of remanence directions residing in the HC-C (geographical coordinates).

There is no clear relation between structures on the map and remanence directions. However, a number of sites connected by a NNE–SSW-trending line show similar remanence directions, which supports the general trend of an anticline structure of the Siang window.

The density plot of in situ directions residing in HC-C (Fig. 12a, b) reveals a trend to clockwise rotations. The degree of clockwise rotations is not confined to a certain magnitude, but spreads over a larger interval with a maximum between about 60 and 125° (density >2.3). The spread in declinations can be partly explained as an artefact created by tilting around sub-horizontal axes after remanence acquisition, but may also indicate that remanence acquisition stretched out over a larger time interval (following India–Asia collision, as long as until the Late Miocene), or that the area consists of sub-units with different degree of clockwise rotation. We assume that the clockwise rotation trend is attributed to the clockwise rotation trend of the eastern Himalayas, which was observed by several palaeomagnetic investigations on Cretaceous to Miocene rocks north and east of the Namche Barwa Syntaxis and is interpreted as the result of ongoing indentation of India into Eurasia (Fig. 15). Increasing clockwise rotations from the western to the eastern part of the central Himalayas were also obtained in a study of secondary Late Eocene to Early Miocene remanences of Tethyan Himalayan meta-sediments (Schill *et al.* 2004). Several numerical models and laboratory experiments on the deformation due to India–Asia collision and ongoing indentation of India into Eurasia have predicted clockwise tectonic rotations around the eastern corner of India (e.g. Houseman & England 1993; Beaumont *et al.* 2001; Cook & Royden 2008). Different models were developed to describe tectonic evolution and uplift of the Tibetan Plateau, such as the 'block model', which assumes that the collision zone is comprised of several lithospheric blocks (e.g. Tapponnier *et al.* 1982; Peltzer & Tapponnier 1988; Avouac & Tapponnier 1993), or those suggesting the existence of a ductile lower crust (e.g. Houseman & England 1996; Royden *et al.* 1997; Beaumont *et al.* 2001; Shen *et al.* 2001). To reveal the relative importance of different models for the evolution of the Tibetan Plateau, palaeomagnetic investigations within the eastern part of the Himalayas are crucial. Our study provides the first such results in the area just south of the Namche Barwa Syntaxis. The continuously distributed maxima of clockwise rotations show that clockwise vertical-axis rotation prevailed at least over the period of remanence acquisition. In comparison to observed rotations in surrounding western or northern areas, the degree of rotation is relatively high (Fig. 15). In consideration that the sampling location is very close to the core of the Namche Barwa Syntaxis, the high degree of rotation is probably due to the high stress rate. Further investigations with a focus on structural control are required in order to get a better insight into the evolution of the eastern Himalayas and the regional tectonic structure of the Siang window.

Conclusions

(1) Detrital zircon fission track thermochronology of the Yinkiong and Miri Fms indicates a post-Paleocene and post-Jurassic age of deposition, respectively, inferring that: (a) the sediment source was located on the overriding Asian plate and/or in the Gangdese thrust belt; and (b) the Abor volcanic rocks intercalating or intruding these sediments are not part of the Upper Palaeozoic sequence as widely proposed in the literature; they must reflect one or more distinct, additional, latest Cretaceous to Tertiary volcanic event(s).

(2) The Siang window rocks (Miri Fm., Abor volcanic series, Yinkiong Fm.) likely shared a common thermal history since Palaeogene times. Early Miocene K–Ar ages of basalt samples are interpreted as partly reset ages representing a post-effusive thermal overprint. Incomplete reset of zircon (U–Th)/He ages suggest maximum temperatures of *c.* 150–180 °C for Late Miocene, implying that the post-depositional thermal overprint did not exceed diagenetic conditions. The detected transformation in magnetic mineralogy is well in line with these results.

(3) Whole rock K–Ar dating of a basalt drift boulder near Sibbum yields an age of 319 $\pm$ 15 Ma and provides geochronological support for the presence of Upper Palaeozoic rocks in the Abor volcanic series.

(4) It can be not excluded that sites with high inclination represent a primary origin during late Palaeozoic times. However, similar rock magnetic properties of all sites are not supportive for variable remanence acquisition ages.

(5) The HC-C shows a trend to clockwise rotations. The inclination only fold test (Enkin & Watson 1996) supports a secondary origin of the remanence component. We assume that remanence acquisition of all sites with directions matching with the clockwise rotation trend occurred during the low temperature overprinting event(s) within in the period of India–Asia collision and Late Miocene. Palaeomagnetic data presented in this paper are compatible with the models of the Tibetan Plateau extrusion. The rotation is not confined to a certain magnitude. The HC-C displays a range of declination values between maxima at about 60° and 125°. This indicates that remanence acquisition was performed over a larger time interval during progressive clockwise rotation, or that the area consists of sub-units with different degree of rotation.

(6) The complex pattern of remanence directions clearly reveals ongoing tectonic deformation after remanence acquisition. Remanence directions support a general NNE–SSW trend of regional structures. The palaeomagnetic results of this paper do not provide an unambiguous interpretation; however, allow some insights into the kinematics of the crust in this geologically highly unexplored area. Further structural and palaeomagnetic

investigations are necessary to unravel the complex regional structure of the Siang window.

Support on the geological investigations by G. Fuchs and P. Blisniuk is kindly acknowledged. We also thank E. Schill, K.V.V. Satyanarayana, P.B. Gawali, and V. Purushotham Rao for field work assistance and sampling. This study was supported by the German Research Foundation (DFG) and by grants from the Indian Institute of Geomagnetism. We thank S. K. Acharyya and C. Crouzet for critical review of the manuscript.

References

ACHARYYA, S. K. 1994. The Cenozoic foreland basin and tectonics of the eastern Sub-Himalaya: problem and prospects. *Himalayan Geology*, **15**, 3–21.

ACHARYYA, S. K. 1998. Thrust tectonics and evolution of domes and the syntaxis in Eastern Himalaya, India. *Journal of Geological Society of Nepal*, **18**, 1–17.

ACHARYYA, S. K. 2005. NE India: a complex terrain of accreted continental blocks. *MGMI, Proc. Sem. Mineral & Energy Resources of Eastern & Northeastern India*. 29–54.

ACHARYYA, S. K. 2007. Evolution of the Himalayan Paleogene foreland basin, influence of its litho-packet on the formation of thrust-related domes and windows in the Eastern Himalayas – A review. *Journal of Asian Earth Sciences*, **31**, 1–17.

ACHARYYA, S. K. & SAHA, P. 2008. Geological setting of the Siang Dome located at the Eastern Himalayan Syntaxis. *Himalayan Journal of Sciences, Special Issue extended abstracts*, **5**, 16–17.

ACHARYYA, S. K. & SENGUPTA, S. 1998. The structure of the Siang Window, its evolution and bearing on the nature of Eastern syntaxis of the Himalaya. *National Academy of Science Letters*, **21**, 177–192.

APPEL, E. 1987. Stress anisotropy in Ti-rich titanomagnetites. *Physics of Earth and Planetary Interiors*, **46**, 233–240.

AVOUAC, J. P. & TAPPONNIER, P. 1993. Kinematic model of active deformation in central Asia. *Geophysical Research Letters*, **20**, 895–898.

BEAUMONT, C., JAMIESON, R. A., NGUYEN, M. H. & LEE, B. 2001. Himalayan tectonics explained by extrusion of a low-viscosity crustal channel coupled to focused surface denudation. *Nature*, **414**, 738–742.

BESSE, J. & COURTILLOT, V. 2002. Apparent and true polar wander and geometry of the geomagnetic field over the last 200 Myr. *Journal of Geophysical Research*, **107**, 2300–2329; doi: 10.1029/2000JB000050.

BHAT, M. I. 1984. Abor volcanics: further evidence for the birth of the Tethys Ocean in the Himalayan segment. *Journal of the Geological Society, London*, **141**, 763–775.

BHAT, M. I. & AHMAD, T. 1990. Petrogenesis and the mantle source characteristics of the Abor volcanic rocks, eastern Himalayas. *Journal of the Geological Society of India*, **36**, 227–246.

BOOTH, A. L., CHAMBERLAIN, C. P., KIDD, W. S. F. & ZEITLER, P. K. 2009. Constraints on the metamorphic evolution of the eastern Himalayan syntaxis from geochronologic and petrologic studies of Namche Barwa. *Geological Society of America Bulletin*, **121**, 385–407.

CHEN, Z., BURCHFIEL, B. C. *ET AL.* 2000. Global Positioning System measurements from eastern Tibet and their implications for India/Eurasia intercontinental deformation. *Journal of Geophysical Research*, **105**, 16215–16227.

CHOWDHURY, J. R. 1979. Abor Volcanics of the Arunachal Himalaya: a discussion. *Journal of the Geological Society of India*, **20**, 45–46.

COGNÉ, J. P., HALIM, N., CHEN, Y. & COURTILLOT, V. 1999. Resolving the problem of shallow magnetizations of Tertiary age in Asia: insights from paleomagnetic data from the Qiangtang, Kunlun and Qaidam blocks (Tibet, China), and a new hypothesis. *Journal of Geophysical Research*, **104**, 17715–17734.

COOK, K. L. & ROYDEN, L. H. 2008. The role of crustal strength in shaping orogenic plateaus, with application to Tibet. *Journal of Geophysical Research*, **113**, B08407, doi: 10.1029/2007JB005457.

DECELLES, P. G., ROBINSON, D. M., QUADE, J., OJHA, T. P., GARZIONE, C. N., COPELAND, P. & UPRETI, B. N. 2001. Stratigraphy, structure, and tectonic evolution of the Himalayan fold-thrust belt in western Nepal. *Tectonics*, **20**, 487–509.

DING, L., ZHONG, D. L., YIN, A., KAPP, P. & HARRISON, T. M. 2001. Cenozoic structural and metamorphic evolution of the eastern Himalayan syntaxis (Namche Barwa). *Earth and Planetary Science Letters*, **192**, 423–438.

DUMITRU, T. A. 1993. A new computer-automated microscope stage system for fission-track analysis. *Nuclear Tracks and Radiation Measurements*, **21**, 575–580.

DUNKL, I. 2002. TRACKKEY: a Windows program for calculation and graphical presentation of fission track data. *Computers and Geosciences*, **28**(1), 3–12.

DUNKL, I., LIN, D. *ET AL.* 2007. *Diagenetic and Metamorphic Overprint and Deformation History of Permo-Triassic Tethyan Sediments, SE Tibet*. 22nd Himalaya–Karakorum–Tibet Workshop, 22–25 May 2007, Hong Kong, abstract volume.

DUPONT-NIVET, G., BUTLER, R. F., YIN, A. & CHAN, X. 2002. Paleomagnetism indicates no Noegene rotation of the Qaidam Basin in northern Tibet during Indo-Asian collision. *Geology*, **30**, 263–266.

ENKIN, R. J. & WATSON, G. S. 1996. Statistical analysis of palaeomagnetic inclination data. *Geophysical Journal International*, **126**, 495–504.

EVANS, N. J., BYRNE, J. P., KEEGAN, J. T. & DOTTER, L. E. 2005. Determination of Uranium and Thorium in Zircon, Apatite, and Fluorite: application to Laser (U–Th)/He Thermochronology. *Journal of Analytical Chemistry*, **60**, 1159–1165.

FARLEY, K. A., WOLF, R. A. & SILVER, L. T. 1996. The effects of long alpha-stopping distance on (U–Th)/He ages. *Geochimica et Cosmochimica Acta*, **60**, 4223–4229.

FISHER, R. A. 1953. Dispersion on a sphere. *Proceedings of the Royal Society of London A*, **217**, 295–305.

FUHRMANN, U., LIPPOLT, H. J. & HESS, J. C. 1987. Examination of some proposed K–Ar standards: $^{40}Ar/^{39}Ar$ analyses and conventional K–Ar-Data. *Chemical Geology. (Isotope Geoscience Section)*, **66**, 41–51, Amsterdam.

FUNAHARA, S., NISHIWAKI, N., MIKI, M., MURATA, F., OTOFUJI, Y. & WANG, Y. Z. 1992. Paleomagnetic study of Cretaceous rocks from the Yangtze block, central Yunnan, China: implications for the India–Asia collision. *Earth and Planetary Science Letters*, **113**, 77–91.

FUNAHARA, S., NISHIWAKI, N., MURATA, F., OTOFUJI, Y. & WANG, Y. Z. 1993. Clockwise rotation of the Red River fault inferred from paleomagnetic study of Cretaceous rocks in the Shan–Thai–Malay block of western Yunnan, China. *Earth and Planetary Science Letters*, **117**, 29–42.

GALBRAITH, R. F. & LASLETT, G. M. 1993. Statistical models for mixed fission track ages. *Nuclear Tracks and Radiation Measurements*, **21**, 459–470.

GANSSER, A. 1964. *Geology of the Himalayas*. Wiley-Interscience, New York.

GANSSER, A. 1974. The Himalayan Tethy*s. Rivista Italiana di Paleontologia e Stratigrafia Memoria*, **14**, 393–411.

GANSSER, A. 1983. Geology of the Bhutan Himalaya. *Denkschriften der Schweizerischen Naturforschenden Gesellschaft*, **96**. Birkhäuser Verlag, Basel.

GLEADOW, A. J. W. 1981. Fission-track dating methods: what are the real alternatives? *Nuclear Tracks*, **5**, 3–14.

GOSWAMI, S., BHOWMIK, S. K. & DASGUPTA, S. 2009. Petrology of a non-classical Barrovian inverted metamorphic sequence from the western Arunachal Himalaya, India. *Journal of the Asian Earth Sciences*, **36**, 390–406.

GREEN, P. F. 1981. A new look at statistics in fission track dating. *Nuclear Tracks*, **5**, 77–86.

GROMMÉ, C. S., WRIGHT, T. L. & PECK, D. L. 1969. Magnetic properties and oxidation of iron-titanium oxide minerals in Alae and Makaopuhi lava lakes, Hawaii. *Journal of Geophysical Research*, **74**, 5277–5293.

GURURAJAN, N. S. & CHOWDHURY, B. K. 2003. Geology and tectonic history of the Lohit valley, Eastern Arunachal Pradesh, India. *Journal of Asian Earth Sciences*, **21**, 731–741.

HALIM, N., COGNÉ, J. P. *ET AL.* 1998. New Cretaceous and early Tertiary paleomagnetic results from Xining-Lanzhou basin, Kunlun and Qiangtang blocks, China: implications on the geodynamic evolution of Asia. *Journal of Geophysical Research*, **103**, 21025–21045.

HEINRICHS, H. & HERRMANN, A. G. 1990. *Praktikum der Analytischen Geochemie*. 669, Springer.

HODGES, K. V., GEISSMAN, J. W. E. & GLAZNER, A. F. E. 2000. Tectonics of the Himalaya and southern Tibet from two perspectives, Special focus on the Himalaya. *Geological Society of America Bulletin*, **112**, 324–350.

HOURIGAN, J. K., REINERS, P. W. & BRANDON, M. T. 2005. U–Th zonation-dependent alpha-ejection in (U–Th)/He chronometry. *Geochimica et Cosmochimica Acta*, **69/13**, 3349–3365.

HOUSEMAN, G. & ENGLAND, P. 1993. Crustal thickening v. lateral expulsion in the Indian–Asian continental collision. *Journal of Geophysical Research*, **98**, 12 233–12 249.

HOUSEMAN, G. & ENGLAND, P. 1996. A lithospheric thickening model for the Indo-Asian collision. *In*: YIN, A. & HARRISON, T. M. (eds) *The Tectonic Evolution of Asia*. Cambridge University Press, New York, 3–17.

HUANG, K. & OPDYKE, N. D. 1993. Paleomagnetic results from Cretaceous and Jurassic rocks of South and Southwest Yunnan: evidence for large clockwise rotations in the Indochina and Shan–Thai–Malay terranes. *Earth and Planetary Science Letters*, **117**, 507–524.

HUANG, K., OPDYKE, N. D., LI, J. & PENG, X. 1992. Paleomagnetism of Cretaceous rocks from eastern Qiangtang terrane of Tibet. *Journal of Geophysical Research*, **97**, 1789–1799.

HURFORD, A. J. 1998. Zeta: the ultimate solution to fission-track analysis calibration or just an interim measure? *In*: VAN DEN HAUTE, P. & DE CORTE, F. (eds) *Advances in Fission-Track Geochronology*. Kluwer Academic Publishers, Dordrecht, 19–32.

HURFORD, A. J. & GREEN, P. F. 1983. The zeta age calibration of fission-track dating. *Chemical Geology (Isotope Geoscience Section)*, **41**, 285–312.

JAIN, A. K. & TANDON, S. K. 1974. Stratigraphy and structure of the Siang district, Arunachal (NEFA), Himalaya. *Himalayan Geology*, **4**, 28–60.

JAIN, A. K. & THAKUR, V. C. 1978. Abor volcanics of the Arunachal Himalaya. *Journal of the geological Society of India*, **19**, 335–349.

JELINEK, V. 1977. The statistical theory of measuring anisotropy of magnetic susceptibility of rocks and its application. *Geofyzika Brno*, 1–88.

KUMAR, G. 1997. Geology of Arunachal Pradesh. *Geological Society of India*, **217**.

KRUIVER, P. P., DEKKERS, M. J. & HESLOP, D. 2001. Quantification of magnetic coercivity components by the analysis of acquisition curves of isothermal remenent magnetisation. *Earth and Planetary Science Letters*, **189**, 269–276.

LE FORT, P. 1975. Himalayas: the collided range. Present knowledge of the continental arc. *American Journal of Science*, **275-A**, 1–44.

LIN, J. & WATTS, D. R. 1988. Palaeomagnetic results from the Tibetan Plateau. *Philosophical Transactions of the Royal Society of London A*, **327**, 239–262.

LOWRIE, W. 1990. Identification of ferromagnetic minerals in a rock by coercivity and unblocking temperature properties. *Geophysical Research Letters*, **17**, 159–162.

MATTAUER, M. 2002. New GPS data in China: a key for a better understanding of the Cainozoic tectonics of Asia. *Comptes Rendus Geoscience*, **334**, 809–810.

MCDOUGALL, I. & HARRISON, T. M. 1999. *Geochronology and Thermochronology by the $^{40}Ar/^{39}Ar$ Method*. Oxford University Press, New York.

MCFADDEN, P. L. 1990. A new fold test for palaeomagnetic studies. *Geophysical Journal Interior*, **103**, 163–169.

MCFADDEN, P. L. & MCELHINNY, M. W. 1995. Combining groups of paleomagnetic directions or poles. *Geophysical Research Letters*, **100**, 316–317.

MOLNAR, P. & TAPPONNIER, P. 1975. Cenozoic Tectonics of Asia: effects of a Continental Collision. *Science*, **189**, 419–426.

O'Reilly, W. 1984. *Rock and Mineral Magnetism*. Blackie, Glasgow and London; Chapman & Hall, New York, **220**.

Otofuji, Y., Inoue, Y., Funahara, S., Murata, F. & Zheng, X. 1990. Palaeomagnetic study of eastern Tibet-deformation of the Three Rivers region. *Geophysical Journal International*, **103**, 85–94.

Otofuji, Y., Liu, Y., Yokoyama, M., Tamai, M. & Yin, J. 1998. Tectonic deformation of the southwestern part of the Yangtze craton inferred from paleomagnetism. *Earth and Planetary Science Letters*, **156**, 47–60.

Pan, G., Ding, J., Yao, D. & Wang, L. 2004. Geological map Qinghai-Xizang (Tibet) Plateau and Adjacent Areas (1:1500000). Chengdu Institute of Geology and Mineral Resources, China Geological Survey. Chengdu Cartographic Publishing House.

Peltzer, P. & Tapponnier, P. 1988. Formation and evolution of strike–slip faults, rifts, and basins during the India–Asia collision: an experimental approach. *Journal of Geophysical Research*, **93**, 15 085–15 117.

Prasad, B., Dey, A. K., Gogoi, P. K. & Maithani, A. K. 1989. Early Permian plant microfossils from the intra-trappean beds of Abor Volcanics, Arunachal Pradesh, India. *Journal of the Geological Society India*, **34**, 83–88.

Reiners, P. W. 2005. Zircon (U–Th)/He Thermochronometry. *Reviews in Mineralogy & Geochemistry*, **58**, 151–179, Mineralogical Society of America.

Reiners, P. W., Spell, T. L., Nicolescu, S. & Zanetti, K. A. 2004. Zircon (U–Th)/He thermochronometry: He diffusion and comparisons with $^{40}Ar/^{39}Ar$ dating. *Geochimica et Cosmochimica Acta*, **68**, 1857–1887.

Royden, L. H., Burchfiel, B. C., King, R. W., Wang, E., Chen, Z., Shen, F. & Liu, Y. 1997. Surface deformation and lower crustal flow in eastern Tibet. *Science*, **276**, 788–790.

Sato, K., Liu, Y., Zhu, Z., Yang, Z. & Otofuji, Y. 1999. Paleomagnetic study of middle Cretaceous rocks from Yunlong, western Yunnan, China: evidence of southward displacement of Indochina. *Elsevier Journal*, **165**, 1–15.

Sato, K., Liu, Y., Wang, Y., Yokoyama, M., Yoshioka, S., Yang, Z. & Otofuji, Y. 2007. Paleomagnetic study of Cretaceous rocks from Pu'er, western Yunnan, China: evidence of internal deformation of the Indochina block. *Earth and Planetary Science Letters*, **258**, 1–15.

Schill, E., Appel, E., Crouzet, C., Gautam, P., Wehland, F. & Staiger, M. 2004. Oroclinal bending v. regional significant clockwise rotations in the Himalayan arc-constraints from secondary pyrrhotite remanences. *In*: Sussman, A. J. & Weil, A. B. (eds) *Orogenic Curvature: Integrating Paleomagnetic and structural analyses*. Geological Society of America, Colorado, Special Paper, **383**, 73–85.

Schumacher, E. 1975. Herstellung von 99,9997% ^{38}Ar für die $^{40}K/^{40}Ar$ Geochronologie. *Geochronologia Chimia*, **24**, 441–442.

Sengupta, S., Acharyya, S. K. & De Smeth, J. B. 1996. Geochemical characteristics of the Abor volcanic rocks, NE Himalaya, India: nature and early Eocene magmatism. *Journal of the Geological Society, London*, **153**, 695–704.

Shen, F., Royden, L. H. & Burchfiel, B. C. 2001. Large-scale crustal deformation of the Tibetan Plateau. *Journal of Geophysical Research*, **106**, 6793–6816.

Shen, Z.-K., Lü, J., Wang, M. & Bürgmann, R. 2005. Contemporary crustal deformation around the southeast borderland of the Tibetan Plateau. *Journal of Geophysical Research*, **110**, B11409, doi: 10.1029/2004JB003421.

Singh, S. 1984. A reappraisal of Yinkiong Formation with reference to Dalbuing area, East Siang district, Arunachal Himalaya. *Indian Minerals*, **38**, 34–38.

Singh, S. 1993. Geology and tectonics of the Eastern Syntaxial Bend, Arunachal Himalaya. *Journal of Himalayan Geology*, **4**, 149–163.

Singh, S. & De, A. K. 1984. An account of Lower Tertiary rocks of East and West Siang districts, Arunachal Himalaya. *Seminar on Recent Advances in Cenozoic Geology of North Eastern Region of India*. Abstracts Book, Dibrugarh.

Singh, S. & Kumar, G. 1990. Basic volcanism in the Arunachal Himalaya and their stratigraphic positions. *Semn. Tectonics and Metallogeny of Ophiolites and recent advances in geology of northeast India. Manipur*, **28** (abstract).

Singh, S. & Malhotra, G. 1987. A note on the basic volcanics of the Siang valley, Arunachal Himalaya. *Indian Minerals*, **41**, 60–63.

Singh, T. 1981. Age and faunal affinity of the Garu Formation, Arunachal Pradesh. *Himalayan Geology*, **10**, 263–270.

Sinha, N. K., Satsangi, P. P. & Misra, U. K. 1986. Paleontology of Permian and Eocene rocks of Siang District, Arunachal Pradesh. *Records of the Geological Survey of India*, **114**, 53–60.

Sol, S., Meltzer, A. S. *et al.* 2007. Geodynamics of the southeastern Tibetan Plateau from seismic anisotropy and geodesy. *Geology*, **35**, 563–566.

Srivastava, P. & Mitra, G. 1994. Thrust geometries and deep structures of the outer and lesser Himalaya, kumaon and Garhwal (India): implications for evolution of the Himalayan fold-and thrust belt. *Tectonics*, **13**, 89–109.

Steiger, R. H. & Jäger, E. 1977. Subcommission on Geochronology: convention on the Use of Decay Constants in Geo- and Cosmochronology. *Earth Planetary Science Letters*, **36**, 359–362.

Tapponnier, P., Peltzer, G., Le Dain, A. Y., Armijo, R. & Cobbold, P. 1982. Propagating extrusion tectonics in Asia: new insights from simple experiments with plasticine. *Geology*, **10**, 611–616.

Tripathi, C. & Chowdhury, R. J. 1983. Gondwanas of Arunachal Himalaya. *Himalayan Geology*, **11**, 73–90.

Tripathi, C., Dungrakoti, B. D. & Ghosh, R. N. 1979. Note on discovery of *Nummulites* from Dihang valley, Siang district, Arunachal Pradesh. *Indian Minerals*, **33**, 43–44.

Tripathi, C., Ghosh, R. N., Gupta, P. D., Malhotra, G. & Dungrakoti, B. D. 1981*a*. Foraminifera from the Siang District, Arunachal Pradesh. *In*: Sinha, A. K. (ed.) *Contemporary Geoscientific Researches in Himalaya*. Bishan Singh Mahendra Pal Singh, Dehra Dun, **1**, 231–242.

TRIPATHI, C., CHOWDHURY, R. J. & DAS, D. P. 1981*b*. Discovery of Tertiary plant fossils from Geku Formation of Dihang valley, Siang district, Arunachal Pradesh. *In*: SINHA, A. K. (ed.) *Contemporary Geoscientific Researches in Himalaya*. Bishen Singh Mahendra Pal Singh, Dehra Dun, **1**, 225–230.

TRIPATHI, C., GAUR, R. K. & SINGH, S. 1988. A note on the occurrence of Nummulitic limestone in East Siang district, Arunachal Pradesh. *Indian Minerals*, **35**, 36–38.

TUCKER, P. & O'REILLY, W. 1980. The laboratory simulation of deuteric oxidation of titanomagnetites: effect on magnetic properties and stability of thermoremanence. *Physics of the Earth and Planetary Interiors*, **23**, 112–133.

WEMMER, K. 1991. K–Ar-Altersdatierungsmöglichkeiten für retrograde Deformationsprozesse im spröden und duktilen Bereich – Beispiele aus der KTB-Vorbohrung (Oberpfalz) und dem Bereich der Insubrischen Linie (N-Italien). *Göttinger Arbeitskreis Geologie/Paläontologie*, **51**, 1–61, Göttingen.

YANG, Z., YIN, J., SUN, Z., OTOFUJI, Y. & SATO, K. 2001. Discrepant Cretaceous paleomagnetic poles between Eastern China and Indochina: a consequence of the extrusion of Indochina. *Tectonophysics*, **334**, 101–113.

YIN, A. 2006. Cenozoic tectonic evolution of the Himalayan orogen as constraint by along-strike variation of structural geometry, exhumation history, and foreland sedimentation. *Earth Science Reviews*, **76**, 1–131.

YIN, A. & HARRISON, M. 2000. Geologic evolution of the Himalayan–Tibetan Orogen. *Annual Review of the Earth and Planetary Sciences*, **28**, 211–280.

YIN, A., DUBEY, C. S., KELTY, T. K., GEHRELS, G. E., CHOU, C. Y., GROVE, M. & LOVERA, O. 2006. Structural evolution of the Arunachal Himalaya and implications for asymmetric development of the Himalayan orogen. *Current Science*, **90**, 195–206.

ZHANG, P.-Z., SHEN, Z., WANG, M., GAN, W., BÜRGMANN, R. & MOLNAR, P. 2004. Continuous deformation of the Tibetan Plateau from global positioning system data. *Geology*, **32**, 809–812.